Original article

Synthesis of nano calcium silicates from waste calcite and aragonite phases for efficient adsorptive removal of industrial organic pollutants

Sumaya Tabassum [a], Md. Sahadat Hossain [a], Mashrafi Bin Mobarak [b], Farah Nigar [a], Samina Ahmed [a,b,*]

[a] Institute of Glass & Ceramic Research and Testing, Bangladesh Council of Scientific and Industrial Research (BCSIR), Dhaka 1205, Bangladesh
[b] BCSIR Dhaka Laboratories, Bangladesh Council of Scientific and Industrial Research (BCSIR), Dhaka 1205, Bangladesh

ARTICLE INFO

ABSTRACT

The present study focuses on the adsorption efficacy of solid-state synthesized calcium silicate for removing congo red dye. Three different sources were used as calcium precursors; one was calcium carbonate, and the other two were natural waste sources, aragonite (*P. globosa*) and calcite (Eggshells). Structural analysis and functional groups of the samples were carried out by X-ray diffractometer (XRD), and a Fourier Transform Infrared Spectrometer (FTIR). Various well-known models/equations models such as the Liner Straight Line method of Scherrer's equation (LSLMSE), Sahadat-Scherrer Model (SSM), Monshi-Scherrer model (MSM), Williamson-Hall model (WHM), Size-Strain plot method (SSP), and Halder-Wagner Model (HWM) were applied to compute the crystallite size of the synthesized calcium silicates; the estimated crystallite size range was 8–77 nm. The adsorption efficacy of the synthesized E-CaSiO$_3$, S-CaSiO$_3$, and C-CaSiO$_3$ was assessed under various provisos for eradicating Congo red dye from wastewater. Computed results revealed that the dye removal percentages were approximately 100 % at 120 min and 200 rpm for 0.2 g E-CaSiO$_3$. The point of zero charge evaluation showed that the pH of the adsorbents during maximum dye removal was 7 and was less than the value of pH$_{pzc}$. Thermodynamics studies confirmed that the adsorption process was spontaneous. The method of adsorption of dye by the adsorbent was more clearly comprehended by Langmuir, Freundlich, and Temkin adsorption isotherm. 151.28 mg/g was the maximum adsorption capacity for S- CaSiO$_3$ depending on the Langmuir isotherm model's linear form (R^2 = 0.924).

1. Introduction

Calcium silicate has diverse applications in several industrial sectors due to its identical properties; such as high chemical stability, thermal stability, corrosion resistance, high-temperature resistance, low thermal conductivity, etc (Palakurthy et al., 2019; Ernawati et al., 2021). They can be used as an adsorbent to remove the dye, as a filling agent in paper, rubber, and plastic, as a milking agent in paint, to shorten the time and baking temperature during the production of ceramic, and so on (Palakurthy et al., 2019; Ernawati et al., 2021).

There are numerous approaches for producing CaSiO$_3$ such as the co-precipitation method, microwave synthesis, sol–gel method, solution combustion method, hydrothermal method, and solid-state reaction (Palakurthy et al., 2019; Abd Rashid et al., 2014). Among all synthesized techniques, the solid-state reaction is preferable and environmentally

friendly because, in this reaction, there is no need for any solvent. A variety of starting materials have been employed in several studies to synthesize CaSiO$_3$ such as Phuttawong *et al.* employed snail shell and rice husk ash (Phuttawong et al., 2015), the picking of eggshell and silica (commercial graded 99 %) was by the team of Vichaphund (Vichaphund et al., 2011), while a choice made by Palakurthy *et al.* was rice husk and eggshell (Palakurthy et al., 2019). Moreover, various temperature was applied by several researchers including Phuttawong *et al.* evaluated the calcination temperature of 800 °C to 1000 °C for the formation of calcium silicate (Phuttawong et al., 2015) while 1100 °C to 1450 °C was selected as a calcination temperature for the synthesis of calcium silicate by Rashid *et al* (Abd Rashid et al., 2014).

Recently, the awareness of environmental issues has renewed interest in minimizing environmental pollution by utilizing natural and waste resources. According to this perspective, in this research work calcite

and aragonite were chosen as a calcium source, and commercially graded $CaCO_3$ was used to compare the efficiency of waste-derived starting materials to synthesize $CaSiO_3$ over the synthetic route. The percentages of calcium carbonate in calcite and aragonite are almost 95 and 97 %, respectively (Sahadat Hossain and Ahmed, 2023).

Nowadays, contamination of water by organic pollutants, dyes, phenolic compounds, pharmaceuticals, and personal care products is a significant environmental concern. Moreover, most industries generate huge amounts of contaminated wastewater during manufacturing. Improper disposal of polluted water causes adverse effects not only on the immediate water body but also on the surrounding environment, including soil, air, and water resources. The contamination of water, not only disrupts the ecosystem but also poses significant hazards like mutagenicity, carcinogenesis, and teratogenicity (Anirudhan et al., 2013; You et al., 2019). However, the treatment of water that contains dye such as organic Congo red is very complicated (Gao et al., 2021). For eradicating dyes from wastewater, multiple strategies have been explored including adsorption (Gao et al., 2021; Nodehi et al., 2020), ultrasound irradiation (Li et al., 2008), photocatalysis (Ali et al., 2020), ion exchange (Jia et al., 2020), mineralization (Diby Paul and Sanjay P Govindwar, n.d.), coagulation-flocculation process (Habiba et al., 2017), electrocatalysis (Wang et al., 2023), biodegradation (Wang et al., 2023), etc. Among all treatment techniques, adsorption is more favorable as a dye removal because this process exhibits high efficiency and is a cost-effective method (Afkhami and Moosavi, 2010; Ghosh et al., 2021; Aryee et al., 2022; Liu et al., 2022). As a result, a lot of investigation was executed to evaluate the adsorption process to purify wastewater by removing congo red (Wang et al., 2023; Han et al., 2022).

This research work has focused on the synthesis of calcium silicate utilizing two waste sources e.g eggshells and snail shells. Snail shells and eggshells are the source of calcium carbonate's naturally formed aragonite and calcite phases. Calcium silicate was also considered an efficient adsorbent for removing congo red dye from a solution that will be applicable for treating industrial wastewater. Moreover, to fully comprehend the characteristics of calcium silicate and its adsorption efficacy, some characterization approaches were also applied.

2. Materials and methods

2.1. Materials

Eggshells were accumulated from the nearby restaurants of the Bangladesh Council of Scientific and Industrial Research, Dhaka, Bangladesh. Snail shells were collected from Tangail. Moreover, 99.5 % pure $CaCO_3$ was used to synthesize the desired product, and this chemical was purchased from a store. To experiment, 99 % silicon di-oxide and distilled water were utilized.

2.2. Methods

Through the solid-state reaction method, calcium silicate was produced by incorporating calcium carbonate and silicon dioxide which can be expressed by the following reaction:

$$CaCO_3 + SiO_2 = CaSiO_3 + CO_2$$
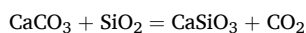
In this experiment, the molar ratio of $CaCO_3$ and SiO_2 was 1:1 and the calcination temperature of the mixture was 1000 °C. To synthesize $CaSiO_3$, commercially graded silicon di-oxide was ground with the powder of calcite, aragonite, and commercially graded calcium carbonate respectively by using a ball mill for 3 h to get homogeneous powder. Then the products were obtained by taking the fine powder into the crucible and placing the crucible in a furnace. The temperature of the furnace was kept at 1000 °C for 4 h. After calcination, the desired products were ground using mortar pastel and stored for further experiment. The overall process for the synthesis of calcium silicate is

portrayed in Fig. 1. The synthesized calcium silicate from three sources was symbolized as E-CaSiO₃ (E-Eggshells), S-CaSiO₃ (S-Snail shells), and C-CaSiO₃ (C-Chemical) during characterizations and application.

3. Characterization of the synthesized products

3.1. Characterization through X-ray diffractometer

The phase and crystallographic parameters were examined through an X-ray diffractometer (Model: Rigaku SmartLab SE). During the scanning, the step size was 0.01 and the results were obtained with a scanning range of $2\theta = 5–70^0$. The XRD machine was operated at 40 kV and 50 mA while the temperature of the chiller was maintained at 20–25 °C. Cu was utilized as a source to generate radiation of CuKα with a wavelength of 1.5406 Å. Silicon was used as a standard reference to calibrate the XRD machine before the analysis of samples. The obtained reflected peaks were identified depending on the standard ICCD database.

3.2. FTIR analysis

The functional groups of the synthesized samples were explored by using the IR-Prestige 21 machine (Shimadzu, Japan) connected to an attenuated total reflection (ATR) to facilitate the FTIR machine. By retaining the spectral resolution of 4 cm^{-1}, the spectrum of the obtained product was captured and the range of the spectrum was 400–4000 cm^{-1} wavenumber. Functioning the IR instrument at a standard temperature, the data was collected from 30 scans on average.

3.3. UV–visible spectrophotometer

The adsorption was measured by employing a UV–visible spectrophotometer (HITACHI, U-2910). The wavelength range was 450–550 nm and an optical glass cuvette was used for the investigation. But during the band gap exploration, 190–350 nm was the wavelength extent and a quartz cell (width 1 cm) was employed. During this investigation, two types of lighting sources (involving tungsten and deuterium lamps) functioned as a source of UV–visible light. The adsorption of the dye onto the adsorbent was measured at a maximum wavelength of 495 nm.

3.4. Study of adsorption

For the experiment of adsorption, 40 mL of 10 ppm dye was taken into 100 mL Erlenmeyer flasks, and 0.1 g adsorbent was added to it. Then the flask was placed in an orbital shaker for shaking at 250 rpm under room temperature for about 180 min. After a fixed time, a UV–Vis spectrophotometer was used to compute the absorbance of the decanted solution that was obtained after the settle down of the adsorbent. To calculate the removal percentage and adsorption capacity equations (1) and (2) were applied, (Hossain et al., 2022)

$$\text{Removal percentage, } R_P = \frac{C_O - C_t}{C_O} \times 100 \quad (1)$$

$$\text{Adsorption capacity, } Q_e = \frac{C_O - C_t}{W} \times V \quad (2)$$

From both equations C_O and C_t are the initial concentration and the final concentration at time t respectively. W reveals the weight of the dry adsorbent and V indicates the volume of the dye solution in milliliters.

4. Results and discussion

4.1. Analysis of phase through XRD

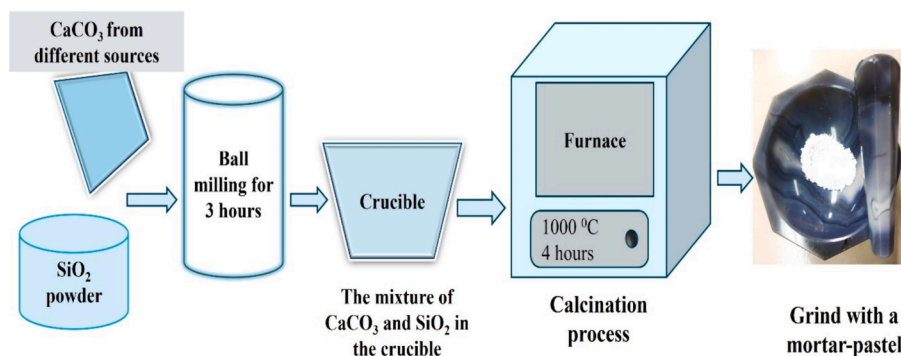To analyze the phase and crystallographic parameters of E-CaSiO₃,

Fig. 1. Flow diagram of the synthesis of calcium silicate from different sources.

C-CaSiO$_3$, and S-CaSiO$_3$, the X-ray diffractometer was used, and the obtained crystallographic phase was correlated with the ICCD database (card no:#00-066-0271). After correlation, the reflected peaks and planes of the three samples are enlisted in Table 1. Consequently, the data in Table 1 confirmed that the synthesized samples from three different sources were calcium silicate and the chemical formula in the ICCD card was CaSiO$_3$. Fig. 2, represents the X-ray diffractogram obtained by examining the synthesized three products.

To analyze the crystallographic parameters, equations (3) to (6) were applied (data are shown in Table 2) to calculate the crystallite size, dislocation density, lattice parameter, microstrain, crystallinity index, and volume of the unit cell respectively (Sahadat Hossain and Ahmed, 2023; Sahadat Hossain et al., 2023).

Size of crystallite, $D_C = \dfrac{K\lambda}{FWHM.cos\theta}$ (3)

Where, D$_C$ = size of crystallite, λ = wavelength (1.4506 Å), K = shape factor (0.90), FWHM = full width at half maxima (in radian), and θ = angle of diffraction (in degree).

Dislocation density, $\delta = \dfrac{1}{(D_C)^2}$ (4)

Where D$_C$ indicates crystallite size.

Microstrain, $\epsilon = \dfrac{FWHM}{4tan\theta}$ (5)

Where FWHM and θ reveal full width at half maxima (in radian) and angle of diffraction (in degree) respectively.

Lattice parameter equation for monoclinic,

$\dfrac{1}{d^2} = \dfrac{1}{sin^2\beta}\left(\dfrac{h^2}{a^2} + \dfrac{k^2sin^2\beta}{b^2} + \dfrac{l^2}{c^2} - \dfrac{2hlcos\beta}{ac}\right)$ (6)

Where, h, k, l = plane of crystals, d = interplanar distance and a, b, c = parameter of lattice

Fig. 2. X-ray diffractogram of synthesized samples.

Table 1
Diffraction peaks and planes of synthesized products with the standard value.

Diffraction angle (2θ)				Planes (h k l)
E-CaSiO$_3$	S-CaSiO$_3$	C-CaSiO$_3$	Standard value (card no: #00–066-0271)	
23.123	23.144	23.218	23.13	4 0 0
25.292	25.334	25.388	25.30	0 0 2
26.880	26.880	26.961	26.86	−2 0 2
28.836	28.896	29.026	28.85	2 0 2
29.953	29.997	30.052	29.95	3 2 0
39.047	39.102	39.153	39.08	−2 0 3
41.231	41.260	41.309	41.27	−4 2 2
49.697	49.813	49.858	49.71	0 4 0

Table 2
Calculated Crystallographic parameters of synthesized samples.

Crystallographic parameters	E-CaSiO$_3$	S-CaSiO$_3$	C-CaSiO$_3$
Crystallite size (nm)	65.24	84.44	49.50
Dislocation density (10^{15} lines per m^2)	0.234	0.14	0.40
Microstrain	0.12	0.0938	0.159
Lattice parameters (Å)	a = 15.43, b = 7.33, c = 7.06	a = 15.40, b = 7.31, c = 7.05	a = 15.29, b = 7.30, c = 7.04

4.2. Calculation of crystallite size

4.2.1. Liner straight-line method of Scherrer's equation

To compute the size of crystallite, the most common and well-known equation is the Liner straight-line equation of Scherrer. The Scherrer equation was reorganized to calculate the crystallite size of the peaks accurately propagated through the XRD analyzer. To determine the crystallite size, the following equation (7) was applied (Henry M. Otte, n.d.; Monshi et al., 2012);

$$cos\theta = \frac{k\lambda}{D_C} \times \frac{1}{\beta} = \frac{K\lambda}{D_L} \times \frac{1}{\beta} \tag{7}$$

From equation (7), θ = diffraction angle in degree, K = shape factor, λ = wave-length of X-ray, D_C = crystallite size, and β = full width at half maxima in radian. The above equation was correlated with a linear straight line (y = mx + c) equation for computing the size of crystallite. To present the above equation in the graph, the value of cosθ (in degree) and 1/β (in radian) was plotted on the y-axis and the x-axis respectively. The size of crystallites was calculated from the slope that was formed due to the above equation and is represented in Fig. 3 (A) for E-CaSiO₃. In the supporting information file, Fig. S_1 (A), and Fig. S_3 (B) are for S-CaSiO₃ and C-CaSiO₃, respectively. The estimated crystallite size was 1388 nm, 3466 nm, and 69327 nm for three different samples that are included in Table 3. This model was not considered applicable due to its larger crystallite size.

4.2.2. Monshi-Scherrer method

The modified version of the Scherrer model known as the Monshi-Scherrer method was constructed by reordering and taking the logarithm on both sides of the Scherrer equation to compute the crystallite size precisely. Mathematically generated Monshi-Scherrer equation can be expressed by equation (8) which was the modification form of the Scherrer equation (7) (Monshi et al., 2012; Nasiri et al., 2023).

$$ln\beta = ln\frac{1}{cos\theta} + ln\frac{K\lambda}{D_M} \tag{8}$$

To ascertain the slope by correlating the above equation with the equation of the straight line (y = mx + c), lnβ, and $ln\frac{1}{cos\theta}$ were plotted on the x-axis as well as on the y-axis respectively. As a result, graphs were generated in Fig. 3 (B), Fig. S_1 (B), and Fig. S_3 (B) for E-CaSiO₃, S-CaSiO₃, and C-CaSiO₃, respectively in which the intercept was $ln\frac{K\lambda}{D_M}$. Through measuring the intercept of equation (8), the size of crystallites was computed for the corresponding three samples that are enlisted in Table 3.

4.2.3. Williamson-Hall method

Scherrer's equation examines the impact of the size of crystallite on XRD peak widening without considering the structural strain of nano-crystals. According to the Williamson-Hall method, the reflection broadening in the XRD pattern is influenced by both crystal size and microstrain (Khorsand Zak et al., 2011). So, depending on the Williamson-Hall method, peak broadening is the sum of strain broadening and size broadening that can be represented by the equation (9),

$$\beta_{total} = \beta_{size} + \beta_{strain} \tag{9}$$

For computing the crystallite size and strain, there are three distinct sub-models depending on the Williamson-Hall method such as the Uniform deformation model (UDM), the Uniform stress deformation model (USDM), and the Uniform deformation energy density model (UDEDM).

4.2.3.1. Uniform deformation model (UDM).

To estimate the crystallite size and strain, the Williamson-Hall model was utilized in that case intrinsic strain was considered (Sahadat Hossain and Ahmed, 2023; Himabindu et al., 2021). The mathematical formula of the Williamson-Hall model has been exposed in equation (10).
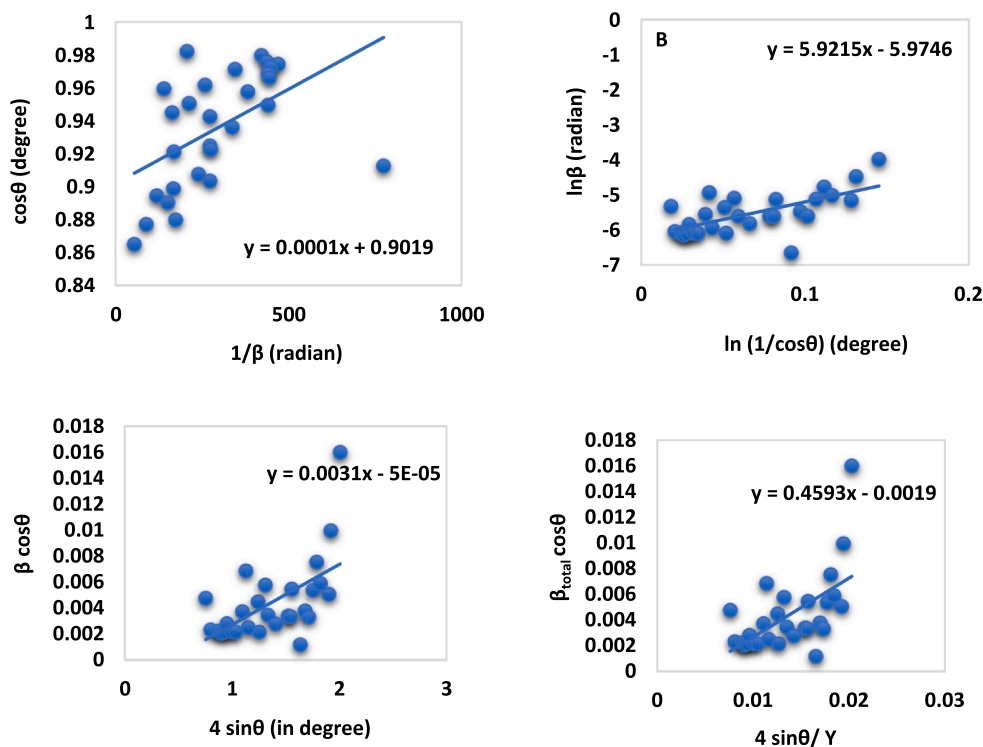

Fig. 3. Ascertainment of the size of crystallite through the linear straight-line model of Scherrer equation (A), Monshi-Scherrer equation (B), Uniform deformation model equation (C), and, Uniform stress deformation model equation (D) for E-CaSiO₃.

Table 3
Estimated crystallite size of three different products depending on several models.

Sample name	Crystal size (nm), Strain (ε), (N/m²), Stress (σ) (N/m²), Energy density (Kj/m³)							
	LSLM	MSM	WHM			SSM	SSP	HWM
			UDM	USDM	UDEDM			
E-CaSiO₃	D = 1386	D = 54	D = 2773 $\varepsilon = 0.0031$	D = 73 $\sigma = 4593 \times 10^5 \varepsilon = 46 \times 10^5$	D = 73 $\mu = 1067$ $\varepsilon = 46.4 \times 10^5$	D = 53	D = 21.66, $\varepsilon = 0.0126$	D = 15.62
S-CaSiO₃	D = 69327	D = 47	D = 37 $\varepsilon = 0.0002$	D = 37 $\sigma = 223 \times 10^5 \varepsilon = 2 \times 10^5$	D = 37 $\mu = 2.42$ $\varepsilon = 2.21 \times 10^5$	D = 77	D = 11.09 $\varepsilon = 0.02$	D = 8
C-CaSiO₃	D = 3466	D = 37	D = 33 $\varepsilon = 0.0002$	D = 33 $\sigma = 1960 \times 10^5 \varepsilon = 1.97 \times 10^5$	D = 33 $\mu = 2$ $\varepsilon = 2.01 \times 10^5$	D = 49	D = 16.50 $\varepsilon = 0.0189$	D = 11.9

$$\beta_{total}cos\theta = \frac{K_B\lambda}{D_W} + 4\varepsilon sin\theta \tag{10}$$

In the plot of β_{total} cosθ against 4sinθ, a linear straight line was generated that was compared with the equation of y = mx + c for calculating the size of crystallites and intrinsic strain. From the calculation, the strain may be a positive or negative value. In that case, when the value of strain is positive, the crystals are in the state of tensile mode (Sahadat Hossain and Ahmed, 2023). On the other hand, compressive strain is the reason for the negative value of the slope that represents the diffraction line moving on the right of the planes (Nasiri-Tabrizi, 2014). The computed crystallite sizes and obtained graphs of several samples are given in Table 3 and Fig. 3 (C), Fig. S_1 (C), and Fig. S_3 (C) for E-CaSiO₃, S-CaSiO₃, and C-CaSiO₃, respectively.

4.2.3.2. Uniform stress deformation model (USDM). Stress because of lattice deformation is assumed to be identical in all directions across the entire crystallite (Mohamed Racik and Hamza Irfan, n.d.). But, according to Hook's law, stress is correlated with strain, and because of the correlation, the obtained mathematical relationship can be represented as, (Khorsand Zak et al., 2011)

$$\sigma = Y_{hkl}.\varepsilon \tag{11}$$

After reorganizing the equation (11)

$$\varepsilon = \frac{\sigma}{Y_{hkl}} \tag{12}$$

Here, ε = strain, σ = stress, and Y_{hkl} = Young's modulus or modulus of elasticity with the value of 99 GPa for wollastonite (Anon, n.d.; Karamanov and Pelino, 2008). Now by putting the strain term in equation (10), the obtained Uniform stress deformation model equation can be expressed the equation (12),

$$\beta_{total}cos\theta = \frac{K_B\lambda}{D_W} + \frac{4.\sigma.sin\theta}{Y_{hkl}} \tag{13}$$

Fig. 3 (D), Fig. S_1 (D), and Fig. S_3 (D) for E-CaSiO₃, S-CaSiO₃, and C-CaSiO₃, respectively, exhibits the plot of equation (13) $\beta_{total}cos\theta$, and $\frac{4.sin\theta}{Y_{hkl}}$ which was plotted on the Y-axis and X-axis respectively. The crystallite size and stress value were computed from the intercept and slope of the straight line respectively and the calculated values are included in Table 3.

4.2.3.3. Uniform deformation energy density model (UDEDM). For real crystals, the two modes of crystal such as anisotropic and isotropic may not be found because of the presence of numerous defects as well as dislocations (Sahadat Hossain and Ahmed, 2023). Consequently, to determine the microstrain and energy density of a crystal, the Uniform deformation energy density model is applied. The energy density can be revealed by equation (14) depending on the Hook's law (Bindu and Thomas, 2014).

$$\mu = \varepsilon^2 \frac{Y_{hkl}}{2} \tag{14}$$

By rearranging the equation (14), the microstrain can be expressed as,

$$\varepsilon = \frac{\sqrt{2\mu}}{\sqrt{Y_{hkl}}} \tag{15}$$

Here, μ = energy density, ε = strain, and Y_{hkl} = Young's modulus or modulus of elasticity with the value of 99 GPa for wollastonite (Anon, n. d.; Karamanov and Pelino, 2008). Now by putting the strain term in equation (10), the obtained Uniform deformation energy density model equation can be expressed in equation (16),

$$\beta_{total}cos\theta = \frac{K_B\lambda}{D_W} + \frac{4.sin\theta.\sqrt{2\mu}}{\sqrt{Y_{hkl}}} \tag{16}$$

To compute the crystallite size and the energy density, $\beta_{total}cos\theta$ and $\frac{4.sin\theta}{\sqrt{Y_{hkl}}}$ were plotted on the X-axis and Y-axis respectively. The crystallite size and strain value were calculated from the intercept and slope of the straight line respectively, and the calculated values are included in Table 3. In addition, the generated graphs after plotting all values are displayed in Fig. 4 (A), Fig. S_2 (A), and Fig. S_4 (A) for E-CaSiO₃, S-CaSiO₃, and C-CaSiO₃, respectively.

4.2.4. Sahadat-Scherrer method
A new model known as the Sahadat-Scherrer model was applied to compute the size of crystallites precisely and the model is based on the Scherrer equation (Sahadat Hossain and Ahmed, 2023). The mathematical expression of the Sahadat-Scherrer model is presented in equation (17). From the Scherrer Equation, a straight line was generated but due to the Sahadat-Scherrer model, a new straight line was formed that passed the origin (Sahadat Hossain and Ahmed, 2023). The Scherrer's equation was improved because of crossing a straight line through the origin that was generated due to the Sahadat-Scherrer model.

$$cos\theta = \frac{K\lambda}{D_{S-S}} \times \frac{1}{FWHM} \tag{17}$$

To build a graph from this model, 1/FWHM and cosθ were plotted on the x-axis and y-axis respectively producing a straight line at the same time an intercept was generated that crossed the origin. To calculate the crystallite size, the generated intercept was correlated with the equation of y = mx + c. The estimated crystallite size from this model is included in Table 3 and the consisted graphs are exhibited in Fig. 4 (B), Fig. S_2 (B), and Fig. S_4 (B) for E-CaSiO₃, S-CaSiO₃, and C-CaSiO₃, respectively.

4.2.5. Size-strain plot method
To evaluate peak broadening in XRD analysis, the crucial aspect is the size of the crystallite and the strain of the lattice. The crystallite size and lattice strain are revealed by the Lorentzian function and Gaussian function respectively (Thool et al., 2014). To estimate the size and strain
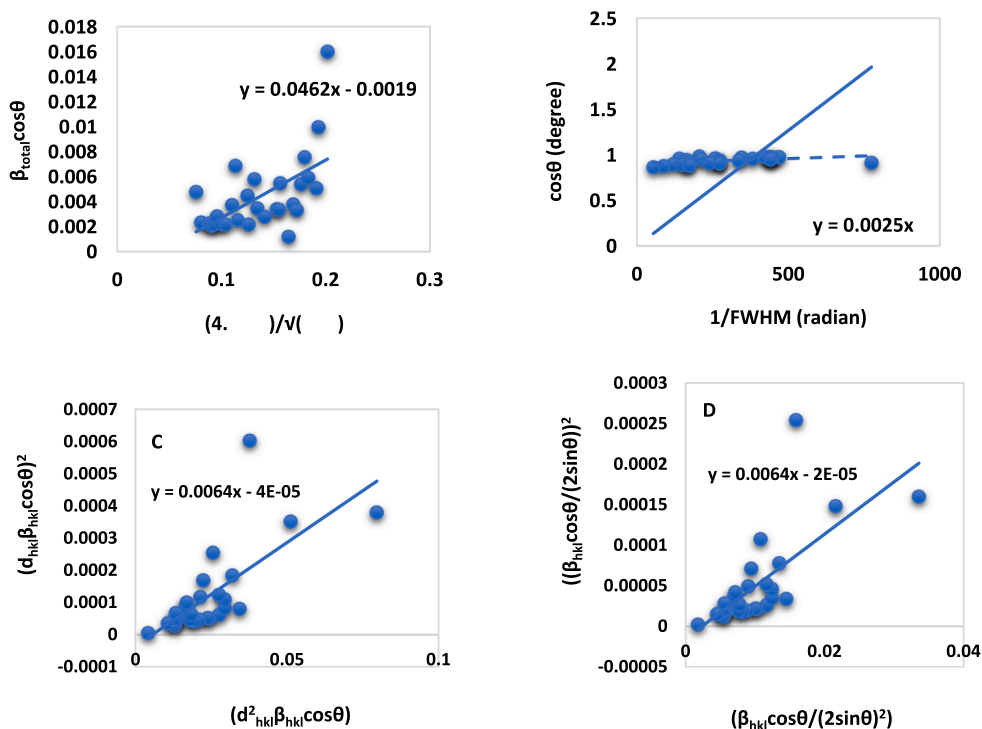
Fig. 4. Ascertainment of the size of crystallite through the Uniform deformation energy density model equation (A), Sahadat-Scherrer equation (B), size-strain plot equation (C), Halder-Wagner equation (D) for E-CaSiO$_3$.

in anisotropic crystal, the size strain plot method was established based on a hypothesis in which a lower angle is more fruitful than a greater angle (Prabhu et al., 2014). So, the crystallite size and strain may be computed precisely by applying a lower angle range of the peaks. The correlation between the size of crystallite and strain based on the Lorentzian function and Gaussian function respectively can be expressed by equations (18), and (19) (Nath et al., 2020; Vinod Kumar, n.d.).

$$\beta_{total} = \beta_L + \beta_G \tag{18}$$

$$(d_{hkl}\beta_{hkl}cos\theta)^2 = \frac{K\lambda}{D}(d_{hkl}^2\beta_{hkl}cos\theta) + \frac{\epsilon^2}{4} \tag{19}$$

Where, d_{hkl} = interplanar distance, β_{hkl} = peak broadening, θ = diffraction angle, K = constant, λ = wavelength on X-ray, D = size of crystallite, and ϵ = strain. $(d_{hkl}^2\beta_{hkl}cos\theta)$ was plotted on the X-axis and $(d_{hkl}\beta_{hkl}cos\theta)^2$ on the Y-axis. After plotting, the obtained graph is given in Fig. 4 (C), Fig. S_2 (C), and Fig. S_4 (C) for E-CaSiO$_3$, S-CaSiO$_3$, and C-CaSiO$_3$, respectively, and the computed crystallite size and strain are included in Table 3.

4.2.6. Halder-Wagner method

In the size-strain plot method, peak profile strain widening was expressed as a Gaussian function, and size broadening as a Lorentz function. Depending on the reciprocal lattice point and cell, Halder-Wagner concocted a new concept to overcome the limitations of the SSP model. According to the Halder-Wagner method, the peak profile was neither a Gaussian function nor a Lorentz function because the XRD peak region matches the Gaussian function while the tail resembles the Lorentz function perfectly (Mohamed Racik and Hamza Irfan, n.d.; Karamanov and Pelino, 2008). Following the assumption of the Halder-Wagner method, Voigt function characterizes peak broadening that can be represented as (Rabiei et al., 2020);

$$\beta_{hkl}^2 = \beta_L\beta_{hkl} + \beta_G^2 \tag{20}$$

$$\left(\frac{{}^*\beta_{hkl}}{{}^*d_{hkl}}\right)^2 = \frac{1}{D_W}\left(\frac{{}^*\beta_{hkl}}{{}^*d_{hkl}^2}\right) + (2\varepsilon)^2 \tag{21}$$

Where β_L and β_G are full widths at half maxima of Lorentz and Gaussian functions respectively. To estimate the crystallite size and intrinsic strain, the Halder-Wagner equation can be expressed as,

$$\left(\frac{\beta_{hkl}cos\theta}{2sin\theta}\right)^2 = \frac{1}{D_W}\left(\frac{\beta_{hkl}cos\theta}{(2sin\theta)^2}\right) + (2\varepsilon)^2 \tag{22}$$

By plotting $\left(\frac{\beta_{hkl}cos\theta}{(2sin\theta)^2}\right)$ and $\left(\frac{\beta_{hkl}cos\theta}{2sin\theta}\right)^2$ on the X-axis and Y-axis respectively (shown in Fig. 4 (D), Fig. S_2 (D), and Fig. S_4 (D) for E-CaSiO$_3$, S-CaSiO$_3$, and C-CaSiO$_3$, respectively), the computed crystallite size and strain from the graph are enlisted in Table 3.

4.3. Exploration of functional group

Fig. 5 represents the characteristics functional group of the synthesized E-CaSiO$_3$, S-CaSiO$_3$, and C-CaSiO$_3$ in their FTIR spectra. At 1000 ^{0}C calcination temperature, the FTIR spectrum of calcium silicate revealed the absorption band at several wavenumbers. For the corresponding three samples, wavenumber ranges 992–1067 cm^{-1} and 643–685 cm^{-1} were due to the asymmetric stretching mode and symmetric stretching vibration of Si-O-Si respectively. Such asymmetric stretching mode and symmetric stretching vibration have been documented in prior investigations (Palakurthy et al., 2019; Li et al., 2016). Absorption bands 898–951 cm^{-1} represented Si-O-Ca bonds with non-bridging oxygen and wavenumber 718 cm^{-1} indicated the stretching mode of O-Si-O bonds. The absorption band at 559 cm^{-1} exhibited Si-O-Si bending vibration whereas 474 cm^{-1} ascribed to the bending mode of O-Si-O and Si-O-Si bonds. The previous literature also revealed similar peaks (Palakurthy
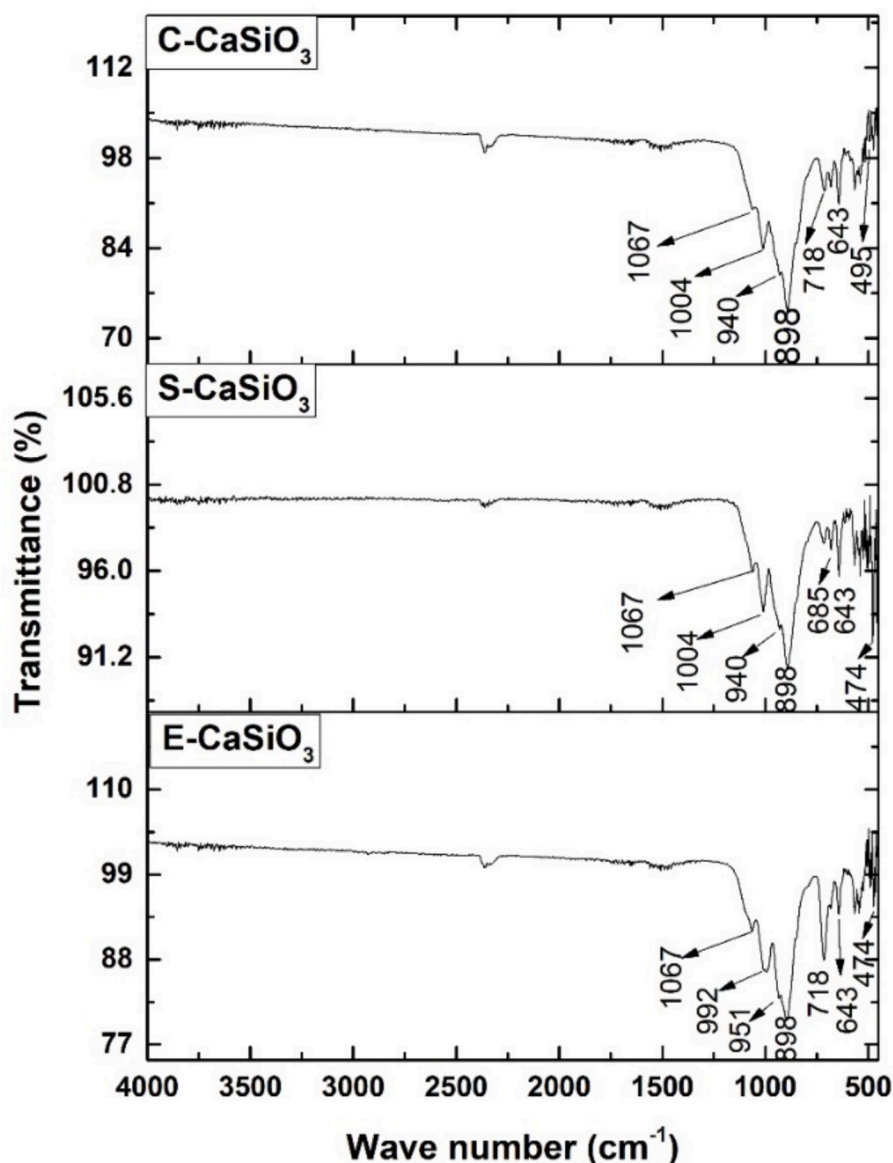
Fig. 5. FTIR spectra of the synthesized E-CaSiO₃, S-CaSiO₃, and C-CaSiO₃.

et al., 2019; Anjaneyulu et al., 2013). In addition, Ca-O stretching vibration occurred at the wavenumber of 495 cm^{-1} which was closely related to the previous study (Ernawati et al., 2021).

4.4. Inspection of optical band gap

The absorption wavelength of the UV–visible spectrophotometer explored the optical band gap of the synthesized E-CaSiO3, S-CaSiO3, and C-CaSiO3. To figure out the optical band gap, a mathematical expression was familiar as the Tauc method which is given in the equation (23) (Mir, 2014; Kaviti and Akkala, 2023);

$$\alpha h\vartheta = A(h\vartheta - Eg)^n \tag{23}$$

From equation (23), α = absorption co-efficient, ϑ = frequency of the photon, h = Plank's constant, A = constant, Eg = band gap energy, and n = 2 or 1/2 in that case 2 for direct band gap and 1/2 for indirect band gap. Through origin software, $h\vartheta$ and $(\alpha h\vartheta)^2$ were plotted on the x-axis and y-axis respectively to estimate the band gap. The computed band gap energy of generated samples is included in Table 4, and the graphical representation is enlisted in the supporting information file

Table 4
Computed band gap energy of synthesized E-CaSiO₃, S-CaSiO₃, and C-CaSiO₃.

Name of the sample	Band gap energy (eV)
E-CaSiO₃	6.18
S-CaSiO₃	6.20
C-CaSiO₃	6.14

(Fig. S_5). There were no significant changes in the band gap of the synthesized three samples.

4.5. Point of zero charge

The point of zero charge (pH$_{pzc}$) is the pH at which the adsorbent's surface charge is zero. The charge of the adsorbent may be positive or negative because it depends on the value of pH and pH$_{pzc}$. When the value of pH becomes less than the value of pH$_{pzc}$, the adsorbent's surface charge will be positive (Ahmad et al., 2012). On the contrary, the adsorbent's surface charge becomes negative when the PH value becomes

more than the value of pH_{pzc}. As a result, a positive charge-carrying adsorbent will interact with anionic dye effectively (Aldahash et al., 2022). To carry out this experiment 0.1 M NaCl (30 mL) was taken with 0.02 g adsorbent in a conical flask. The initial pH_i (5, 7, 9, and 11) of this mixture was maintained by adding 1 M HNO_3 and 0.25 M NaOH. Then the conical flask was placed for shaking for 30 min in the orbital shaker. After 30 min, again the pH_f of the sample was checked to evaluate the ΔpH ($\Delta pH = pH_f - pH_i$). By plotting pH_i, and ΔpH on the X-axis, and Y-axis, respectively; a line with a point of intersection (Fig. 6) was found from which the value of pH_{pzc} was explored. The pH_{pzc} values of the synthesized E-CaSiO$_3$, S-CaSiO$_3$, and C-CaSiO$_3$ are 8.4, 7.9, and, 8.1, respectively. The maximum removal percentage was found at pH 7 in the batch experiment for the three categories of adsorbent. The pH was lower than the values of pH_{pzc}, so the positively charged adsorbent surface interacted with anionic congo red dye more effectively.

4.6. Studies of adsorption

4.6.1. Effect of time interval on adsorption

Time has an impact on adsorption efficacy so the removal percentage and adsorption capacity will change due to the variation of time. The removal percentage and adsorption capacity for E-CaSiO$_3$, S-CaSiO$_3$, and C-CaSiO$_3$ escalated dramatically with increasing time. The maximum removal percentage was 97 % for 0.1 g C-CaSiO$_3$ at a time of 180 min whereas the minimum one was 79 % for 0.1 g C-CaSiO$_3$ at a time of 60 min. Fig. 7 illustrates that at 120 and 180 min, the removal percentages were almost identical. This happens as a result of dye molecules inhibiting the adsorbent's active sites over time (Adeogun et al., 2018). Consequently, a balance was revealed.

4.6.2. Impact of shaking speed

Due to the variation of the speed of the orbital shaker (rpm), the adsorbent interacted with the adsorbate properly. Consequently, with increasing speed, the percentage of removal and adsorption capacity was changed moderately. For E-CaSiO$_3$ and S-CaSiO$_3$, the removal percentage and adsorption capacity climbed significantly due to the elevation of speed but at the speed of 250 rpm, the value fell modestly. This phenomenon happens because the kinetic energy between the dye molecules and the adsorbent particles is enhanced when increasing the shaking speed. Consequently, the contact also intensifies, thereby enhancing the adsorption capacity. Following optimal circumstances,

both the adsorbent and the adsorbate have higher kinetic energies, but the adsorbent molecules become apart from the least constrained dye molecules (Jamil et al., 2014). 98 % and 61 % were the maximum and minimum removal percentages respectively for 0.1 g S- CaSiO$_3$ adsorbent at the speed of 200 rpm and 50 rpm respectively. Fig. 8 represents the removal percentage and adsorption capacity for different speeds (rpm).

4.6.3. Effects of different doses of adsorbent

The effect of adsorbent doses on the removal percentage and adsorption capacity was observed by taking various doses of adsorbent that limit was 0.025 to 0.3 g. With raising adsorbent doses, the percentage of removal went up substantially for the three different adsorbents but it dropped a bit due to the 0.3 g adsorbent. The highest removal percentage was fairly 99 % for 0.1 g of C-CaSiO$_3$ adsorbent as well and the lowest one was 73 % for 0.05 g of E-CaSiO$_3$ adsorbent. For 0.2 g of adsorbent, the removal percentage was more than 0.3 g of adsorbent. In that case, the adsorbents are agglomerated in the case of 0.3 g of adsorbent. As a result, the adsorbent's active sites are mitigated, and the dye removal percentage likewise drops (You et al., 2019). In addition, adsorption capacity dropped gradually with increasing the amount of catalyst and the maximum was 14.920 mg/g for 0.025 g C-CaSiO$_3$. For additional inspection, 0.2 g adsorbent, 180 min, and 200 rpm were taken as fixed depending on the percentage of removal and adsorption capacity. Fig. 9 represents the removal percentage and adsorption capacity for diverse adsorbent doses.

4.6.4. Impact of different dye concentrations

To observe the effect of dye concentration on the removal percentage and adsorption capacity, several dye concentrations were chosen for experiments. For this purpose, some parameters were static as previously mentioned. With rising dye concentrations, the removal percentage fluctuated, and the maximum was approximately 100 % for E-CaSiO$_3$ adsorbent. For the S-CaSiO$_3$ adsorbent, the removal percentage and adsorption capacity climbed modestly but the percentage declined dramatically because of the increasing concentration of dye. The removal percentage for C-CaSiO$_3$ rose and fell due to the variation of concentration of dye and the maximum removal percentage was 99 % at 30 ppm. The dye removal percentage falls gradually with rising dye concentration. This happens because the molecules of dye block the active site of the adsorbents (Bin Mobarak et al., 2023). As a result, the
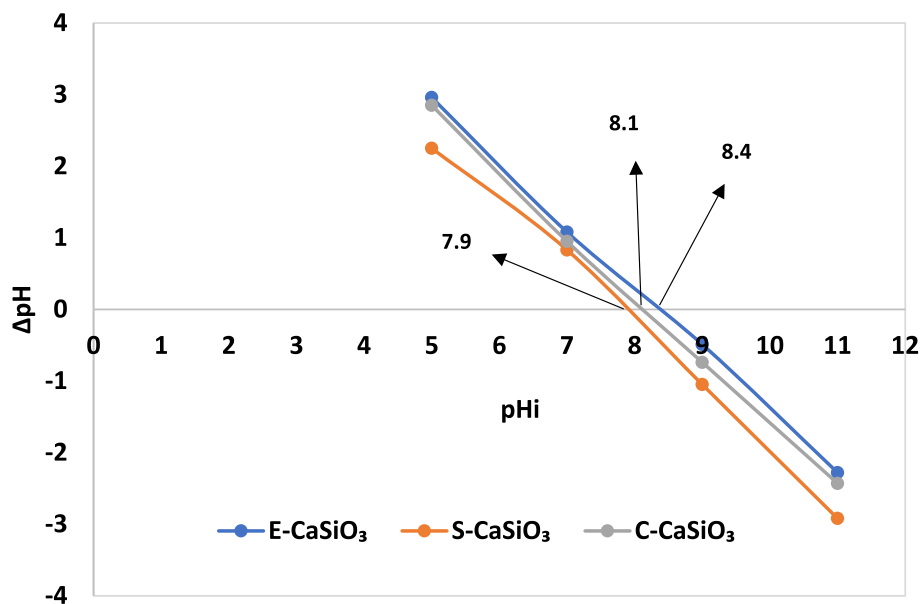

Fig. 6. Point of zero charges of the synthesized E-CaSiO$_3$, S-CaSiO$_3$, and C-CaSiO$_3$.
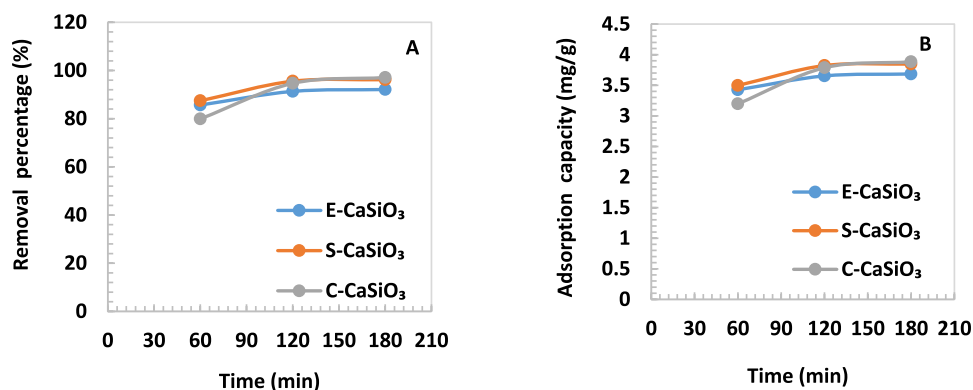
Fig. 7. (A) Removal percentage and (B) Adsorption capacity of 0.1 g adsorbent in terms of time variation.
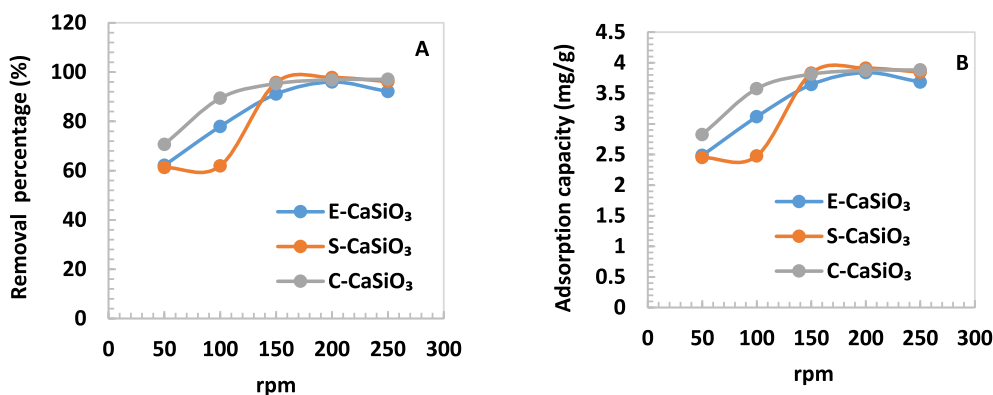

Fig. 8. (A) Removal percentage and (B) Adsorption capacity of 0.1 g adsorbent in terms of several speeds (rpm).
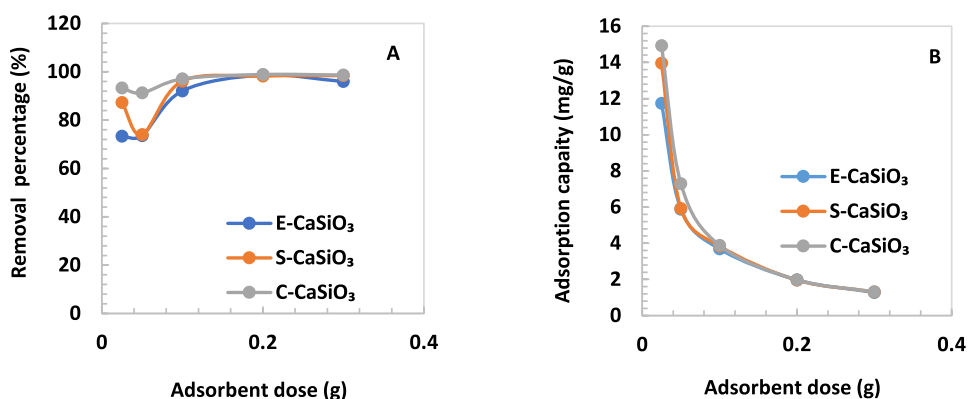

Fig. 9. (A) Removal percentage and (B) Adsorption capacity of several adsorbent doses at a fixed speed of 200 rpm and time of 180 min.

interaction between dye molecules and adsorbent declines with increasing the concentration of dye. The impact of several dye concentrations on removal percentage and adsorption capacity is represented in Fig. 10.

4.6.5. Effect of several pH limits

The removal percentage and adsorption capacity are significantly influenced by the solution's different pH limits. Fig. 11 displays that for E-CaSiO$_3$, the removal percentage and adsorption capacity rose minimally but it came down at pH 9. This phenomenon occurs as a result of the adsorbent surface becoming positively charged when the pH level is low. At lower pH, H$^+$ ions induce surface active sites to become protonated (Nath et al., 2021). Inevitably, the surface of the adsorbent becomes positively charged. Conversely, the surface of the adsorbent

turns into a negative charge at high pH due to the presence of OH$^-$ ions (Jamil et al., 2014). Congo red is an anionic dye, so the conjunction between the molecules of dye (negatively charged) and adsorbent (positively charged) becomes strong (Al-Degs et al., 2008). Consequently, the removal percentage of dye becomes higher when the pH level is low. At pH 7, the maximum removal percentage was 97 % to nearly 99 % for the E-CaSiO$_3$, S-CaSiO$_3$, and C-CaSiO$_3$. Moreover, to prepare a pH 7 solution, there was no need to add extra acid or base for this reason pH 7 was kept fixed.

4.7. Adsorption isotherm

Through isotherm models, it is possible to assess the equilibrium adsorption data. Moreover, adsorption isotherm models can convey
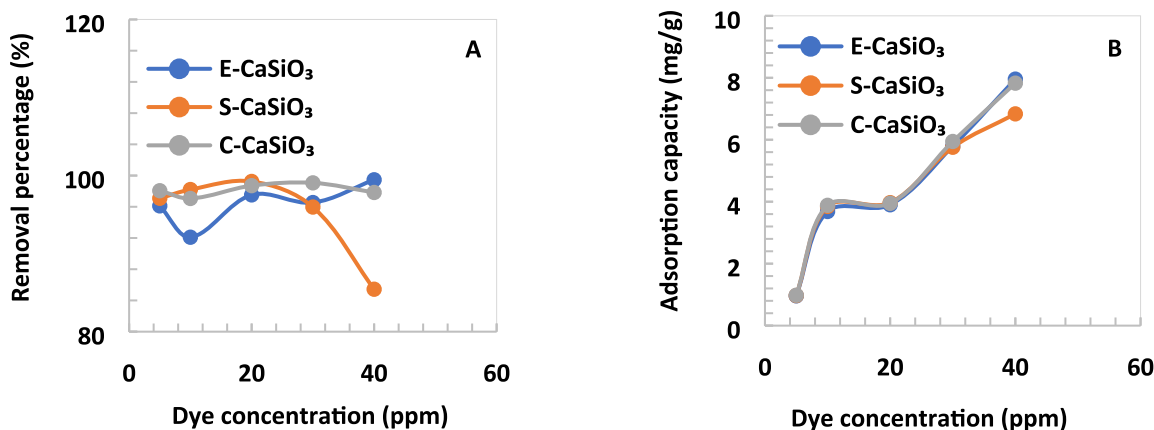
Fig. 10. (A) Removal percentage and (B) Adsorption capacity of several dye concentrations at a fixed speed of 200 rpm, time of 180 min, and amount of adsorbent 0.2 g.
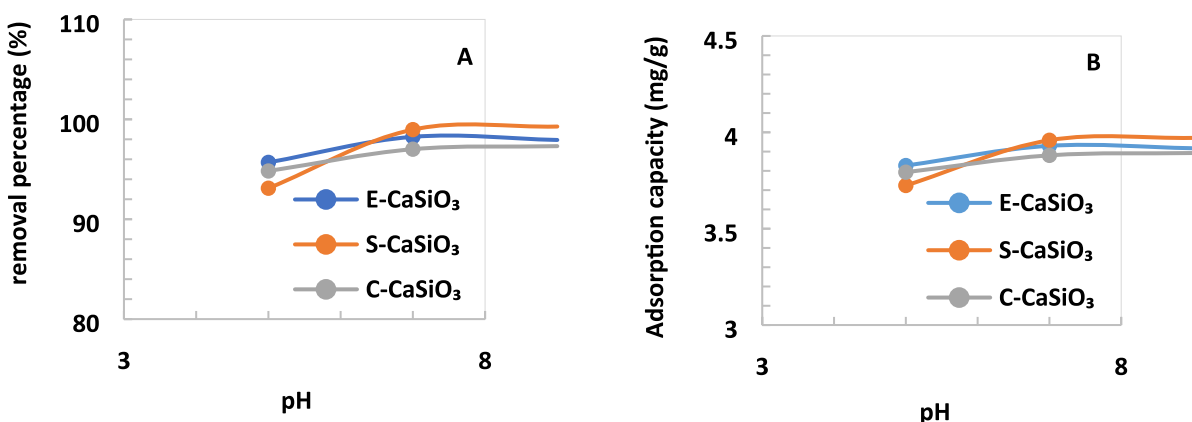

Fig. 11. (A) Removal percentage and (B) Adsorption capacity of 0.2 g adsorbent at a fixed speed of 200 rpm, time of 180 min under various pH limits.

qualitative information about the adsorption capacity of adsorbents. To evaluate the adsorption equilibrium data in the case of adsorption of Congo red dye onto the surface of the desired product, Langmuir adsorption isotherm (including linear and non-linear), Freundlich isotherm (involving linear and non-linear), and Temkin isotherm were frequently employed.

4.7.1. Langmuir adsorption isotherm

4.7.1.1. Linear form of Langmuir adsorption isotherm. The linear form of Langmuir adsorption isotherm is presented in the equation (24), (Hu et al., 2017)

$$\frac{1}{q_e} = \frac{1}{K_L q_{max}} \times \frac{1}{C_e} + \frac{1}{q_{max}} \tag{24}$$

Where, q_e = equilibrium concentration of Congo red adsorbed (mg/g), C_e= equilibrium concentration of Congo red in the solution (mg/L), q_{max} = maximum adsorption capacity of the synthesized product (mg/g), and K_L = constant of the Langmuir isotherm model (mg/L). After plotting $1/C_e$ and $1/q_e$ on the X-axis and Y-axis respectively, a straight line was generated (displayed in Fig. 12). By comparing the generated straight line with the straight equation (y = mx + c), the value of slope and intercept were estimated by Origin Pro 9 software which is enlisted in Table 5. Depending on the Langmuir adsorption constant (K_L), the

dimensionless equilibrium parameter (R_L) was calculated by applying equation (25) (Hossain et al., 2022).

$$R_L = \frac{1}{1 + K_L C_{max}} \tag{25}$$

Here, C_{max} reveals the maximum initial concentration of dye. Depending on the dimensionless equilibrium parameter (R_L), the situation of adsorption can be expressed such as $R_L = 1$ reveals the linear isotherm and $0 < R_L < 1$ indicates appropriate adsorption. Moreover, $R_L > 1$ and $R_L = 0$ explain disagreeable and irreversible adsorption respectively (Bin Mobarak et al., 2023).

4.7.1.2. Non-linear form of Langmuir adsorption isotherm. The non-linear form of Langmuir adsorption isotherm equation is revealed in the equation (26), (Pinky et al., 2023; Salihi, n.d.)

$$q_e = \frac{Q_m \times K_L \times C_e}{1 + K_L \times C_e} \tag{26}$$

Here, Q_m is the maximum adsorption capacity of the synthesized product. Through plotting C_e and q_e on the X-axis and Y-axis respectively, a straight line was generated (exhibited in Fig. 13) that was compared with the straight-line equation (y = mx + c) for estimating the value of slope and intercept. The obtained values through Origin Pro 9 software are given in Table 5 and after fitting (linear and non-linear) all
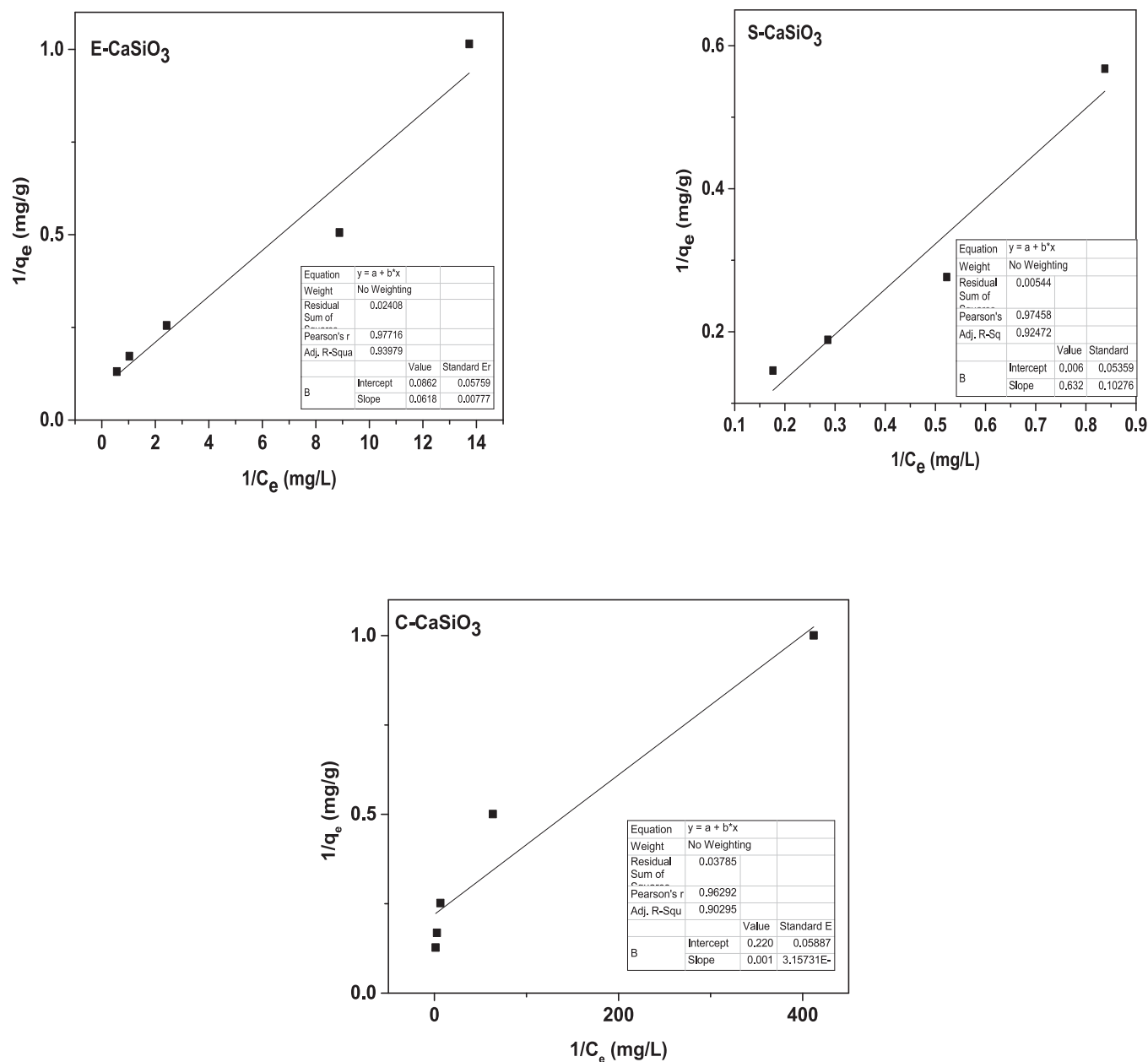
Fig. 12. Graphical representation of the linear form of Langmuir adsorption isotherm.

calculated values are included in Table 6.

4.7.2. Freundlich isotherm

4.7.2.1. Linear form of Freundlich adsorption isotherm.
Through the Freundlich adsorption isotherm equation, it is possible to evaluate the heterogeneous surface with multilayer adsorption. Mathematically the equation can be expressed as,

$$\frac{x}{m} = K_f C_e^{\frac{1}{n}} \tag{27}$$

By taking logarithms on both sides of the equation (27), the newly formed equation can be presented as,

$$\log\frac{x}{m} = \log K_f + \log(C_e)^{\frac{1}{n}} \tag{28}$$

$$\log\frac{x}{m} = \log K_f + \frac{1}{n}\log C_e \tag{29}$$

By rearranging equations (28) and (29), the Linear form Freundlich isotherm of the equation will be, (Bagal and Raut-Jadhav, 2021)

$$\log q_e = \log K_f + \frac{1}{n}\log C_e \tag{30}$$

Here, K_f = Freundlich constant (mg/L), n = constant of the intensity of the adsorption, q_e = adsorption capacity (mg/g), and C_e = adsorbate concentration (mg/L). The value of n explains the adsorption process including an intricate adsorption process (n < 1), relatively complicated adsorption (1 < n < 2), or favorable adsorption (2 < n < 10) (Pinky et al., 2023; Shayesteh et al., 2016). By plotting $\log C_e$ on the X-axis and $\log q_e$ on the Y-axis, a straight was produced that is represented in Fig. 14. After plotting, the slope and intercept were obtained by applying Origin Pro 9 software, and all the obtained values are enlisted in Table 5.

4.7.2.2. Non-linear form of Freundlich adsorption isotherm.
The non-linear form of the Freundlich adsorption isotherm equation can represented by the following equation, (Vitek and Masini, 2023)

Table 5

Obtained values depending on isotherm model through Origin pro 9 software for 0.2 g of E-CaSiO$_3$, S-CaSiO$_3$, and C-CaSiO$_3$ samples.

Isotherm model	Fitting of curve	Sample name	Intercept value	Slope value	Adj. R-Square
Langmuir	Linear	E-CaSiO$_3$	0.08625	0.06188	0.93979
		S-CaSiO$_3$	0.00661	0.63223	0.92472
		C-CaSiO$_3$	0.22011	0.00195	0.90295
	Non-linear	E-CaSiO$_3$	10.02532	1.60597	0.98448
		S-CaSiO$_3$	15.90793	0.13716	0.96343
		C-CaSiO$_3$	9.33832	5.58132	0.88791
Freundlich	Linear	E-CaSiO$_3$	0.77206	0.59628	0.94392
		S-CaSiO$_3$	0.24324	0.84031	0.90799
		C-CaSiO$_3$	0.92303	0.35313	0.99547
	Non-linear	E-CaSiO$_3$	5.77164	1.93296	0.98345
		S-CaSiO$_3$	2.04386	1.40002	0.9404
		C-CaSiO$_3$	8.68647	2.63548	0.9939
Temkin	Linear	E-CaSiO$_3$	6.09899	1.97872	0.97985
		S-CaSiO$_3$	1.3251	3.20938	0.99327
		C-CaSiO$_3$	7.16597	1.12937	0.87933

$$q_e = K_f(C_e)^{1/n} \tag{31}$$

The value of C_e and q_e were plotted on the X-axis and Y-axis respectively. After plotting, the generated graphs are represented in Fig. 15 and yielded all values from Origin Pro 9 software given in Table 5. Moreover, the computed parameters after linear and non-linear fitting are enlisted in Table 6.

4.7.3. Temkin isotherm model

The Temkin isotherm equation is mathematically expressed by the equation (34) (Anon (2), n.d.);

$$q_e = \frac{RT}{b}\ln(A_T C_e) \tag{32}$$

$$q_e = \frac{RT}{b}\ln(A_T) + \frac{RT}{b}\ln(C_e) \tag{33}$$

$$q_e = B_T\ln(A_T) + B_T\ln(C_e) \tag{34}$$

Here, b = Temkin isotherm constant, $B_T = \frac{RT}{b}$ = constant connected to the heat of adsorption (J/mol), A_T = Temkin isotherm equilibrium binding constant (L/mg), R = universal gas constant (J/mol K), and T = temperature (K). Now by placing the values of $\ln(C_e)$ on the X-axis and q_e on the Y-axis, a straight line was generated after linear fitting which is presented in Fig. 16. The estimated isotherm parameters after fitting are included in Table 6.

4.7.4. Thermodynamics studies

The thermodynamic parameter ΔG^0 (standard Gibbs free energy) was calculated utilizing equation (35) which comprehends the mode of adsorption on the synthesized adsorbent (Ghasemi et al., 2014).
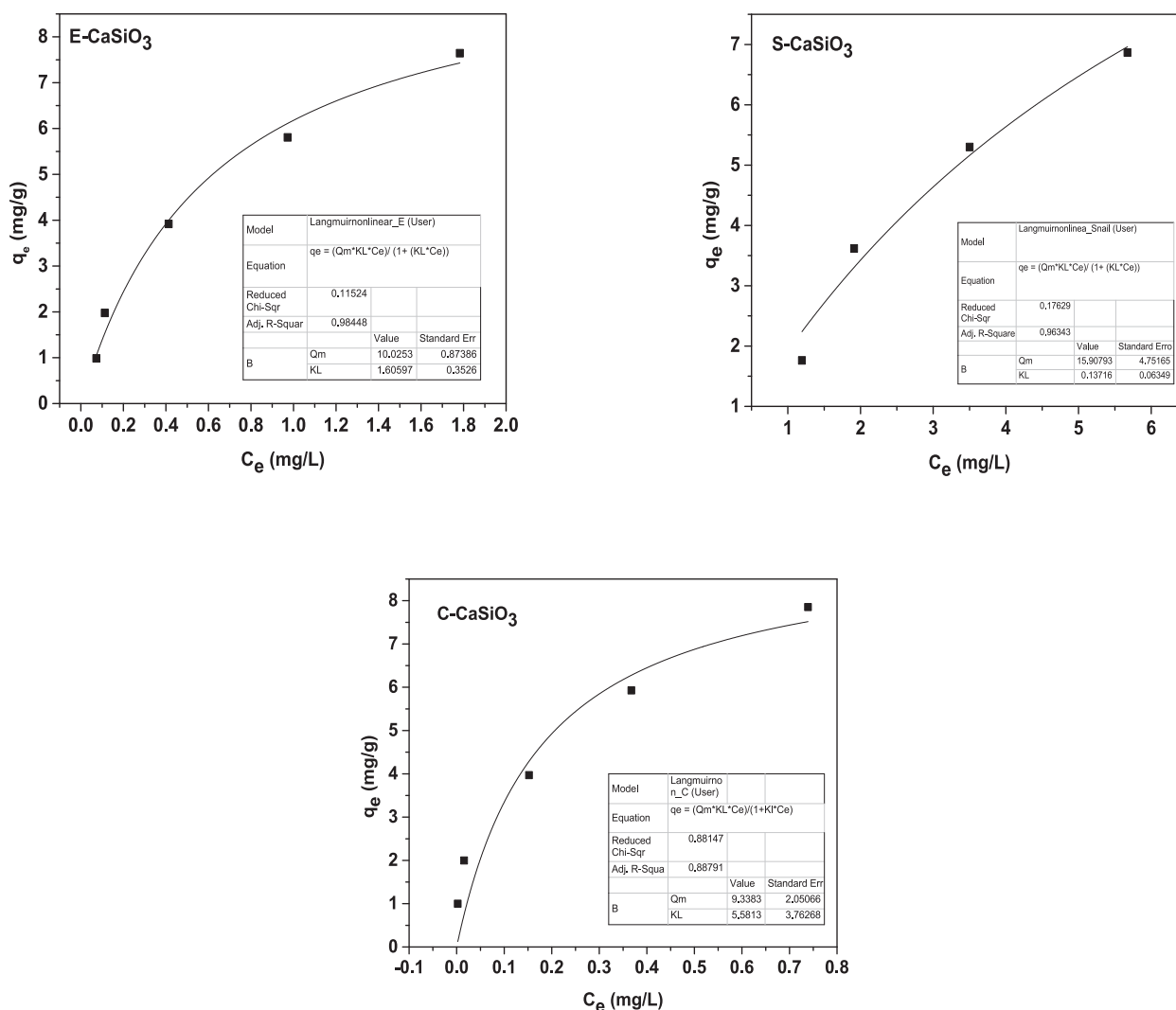

Fig. 13. Graphical representation of the non-linear form of Langmuir adsorption isotherm.

Table 6
Estimation of isotherm parameters for the adsorption of dye onto the adsorbent.

Isotherm model	Fitting of curve	Sample name	Parameters value		
			q_m (mg/g)	K_L (mg/L)	R_L
Langmuir	Linear	E-CaSiO$_3$	11.59420	1.39382	0.07048
		S-CaSiO$_3$	151.28593	0.01045	0.70511
		C-CaSiO$_3$	4.54318	113.16044	0.00022
	Non-linear	E-CaSiO$_3$	10.02532	1.60597	–
		S-CaSiO$_3$	15.90793	0.13716	–
		C-CaSiO$_3$	9.33832	5.58132	–

		Sample name	Parameters value	
			K_f (mg/L)	n
Freundlich	Linear	E-CaSiO$_3$	5.91643	1.67706
		S-CaSiO$_3$	1.75081	1.19003
		C-CaSiO$_3$	8.37587	2.83181
	Non-linear	E-CaSiO$_3$	5.77164	1.93296
		S-CaSiO$_3$	2.04386	1.40002
		C-CaSiO$_3$	8.68647	2.63548

		Sample name	Parameters value	
			B_T (J/mol)	A_T (L/mg)
Temkin	Linear	E-CaSiO$_3$	1.97872	21.8083
		S-CaSiO$_3$	3.209	1.511196
		C-CaSiO$_3$	1.1293	569.8854

$$\Delta G^0 = -RT \ln K \qquad (35)$$

In equation, ΔG^0 = standard Gibbs free energy (KJ/mol), T = absolute temperature (298 K), R = universal gas constant (8.314 Jmol^{-1} K^{-1}), and K = thermodynamic equilibrium constant derived from several isotherm models (Langmuir, Freundlich, and Temkin isotherm model).

The computed values of ΔG^0 are enlisted in Table 7. The negative ΔG^0 values signified that the adsorption onto the adsorbent was thermodynamically effective. Moreover, it indicated the spontaneous adsorption process (Ebisike et al., 2023). The ΔG^0 values for the adsorbents were negative according to Langmuir, Freundlich, and Temkin isotherm models. But the ΔG^0 values of S-CaSiO$_3$ adsorbent were positive in the case of Langmuir linear and non-linear isotherm model so the adsorption process was not spontaneous. A comparative study between the present work and the previous work is registered in Table 8.

4.7.5. Regeneration and reusability test

For preserving the environment and considering monetary feasibility, the reusability of adsorbent is a crucial factor. The reusability activity of the synthesized adsorbent (E-CaSiO$_3$, S-CaSiO$_3$, and C-CaSiO$_3$) was observed which is depicted in Fig. 17. This figure represents that the three adsorbents maintained their active behavior following the cycle of regeneration. For this experiment, 0.2 g of adsorbent, and 20 ppm of congo red dye solution (40 mL) were placed in a conical flask.
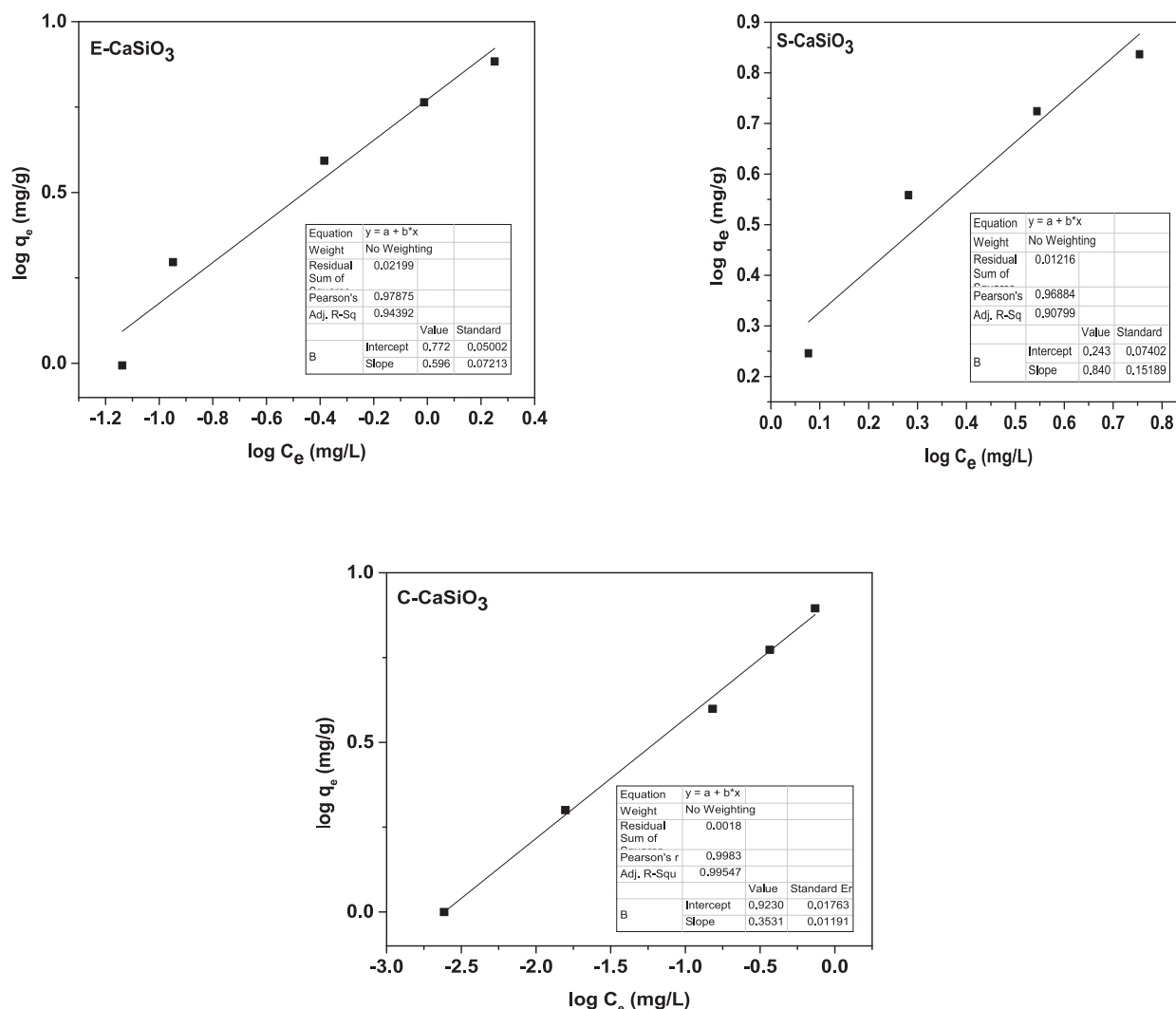

Fig. 14. Graphical representation of the linear form of Freundlich adsorption isotherm.

E-CaSiO$_3$

Model	E_Freundlich_nonlinear (User)		
Equation	qe = Kf* (Ce)^(1/n)		
Reduced Chi-Sqr	0.12287		
Adj. R-Squar	0.98345		
		Value	Standard Err
B	Kf	5.7716	0.19225
	n	1.9329	0.16718

S-CaSiO$_3$

Model	Freundlichnonlinear_Snail (User)		
Equation	qe = Kf*(Ce)^(1/n)		
Reduced Chi-Sqr	0.28732		
Adj. R-Squ	0.9404		
		Value	Standard E
B	Kf	2.043	0.35727
	n	1.400	0.23617

C-CaSiO$_3$

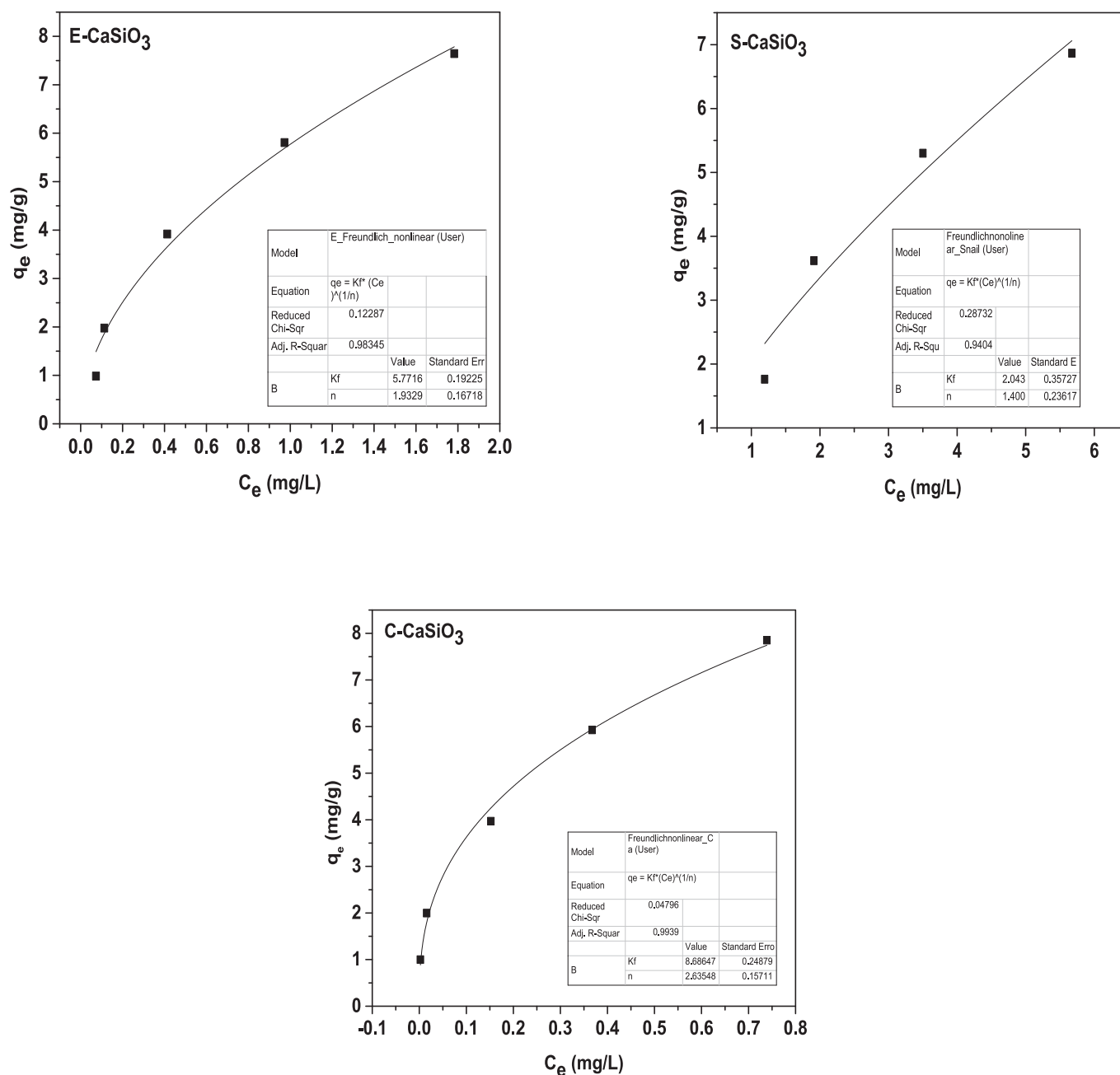| Model	Freundlichnonlinear_Ca (User)		
Equation	qe = Kf*(Ce)^(1/n)		
Reduced Chi-Sqr	0.04796		
Adj. R-Square	0.9939		
		Value	Standard Erro
B	Kf	8.68647	0.24879
	n	2.63548	0.15711

Fig. 15. Graphical representation of the non-linear form of Freundlich adsorption isotherm.

Afterward, the solution was agitated on an orbital shaker at a speed of 200 rpm for 180 min. Three cycles were carried and the adsorbent was washed with deionized water after each cycle. After washing, the adsorbent was dried in an oven at 100 °C for 2 h for the next cycle. The removal percentage was above 97 % for the three adsorbents in the first cycle. But it dropped gradually in the third cycle; the removal percentage became 80 %, 67 %, and 72 % for E-CaSiO$_3$, S-CaSiO$_3$, and C-CaSiO$_3$, respectively. At the same, the adsorption capacity decreased modestly. This happened due to the removal of active SiO$_2$ during washing after each cycle as reported in the previous literature (Zhao et al., 2017).

4.7.6. Adsorption mechanism

The strong electrostatic attraction between the dye's negative charge and the adsorbent's positive charge can interpret the adsorption mechanism of congo red dye and adsorbent. The interaction between adsorbent and adsorbate occurs due to hydrogen bonding and ion exchange (Adebayo et al., 2022). Hydrogen bonding mainly happens between hydrogen atoms of dye and the SiO$_3$ part of CaSiO$_3$, whereas ion exchange occurs between CaSiO$_3$ (adsorbent) and dye solution ions. The Ca part of CaSiO$_3$ can form a chelation bond with the sulfonate, amino, or azo groups on the surface of the adsorbent (Bin Mobarak et al., 2023). The dye can cling to the surface of the adsorbent by an interchanging mechanism. The overall adsorption mechanism is portrayed in Fig. 18.

4.7.7. FTIR analysis after the adsorption and recycling process

The functional group of the synthesized E-CaSiO$_3$, S-CaSiO$_3$, and C-CaSiO$_3$ after adsorption of congo red dye (A) and after recycling three cycle steps (B) are portrayed in Fig. 19. The functional groups of the adsorbent after the adsorption process and after the reusability test were mostly similar to the FTIR data of the raw adsorbent except band at 1473 cm^{-1}. The absorption band at 1473 cm^{-1} revealed the stretching vibration of N = N due to the presence of congo red dye. The reason for
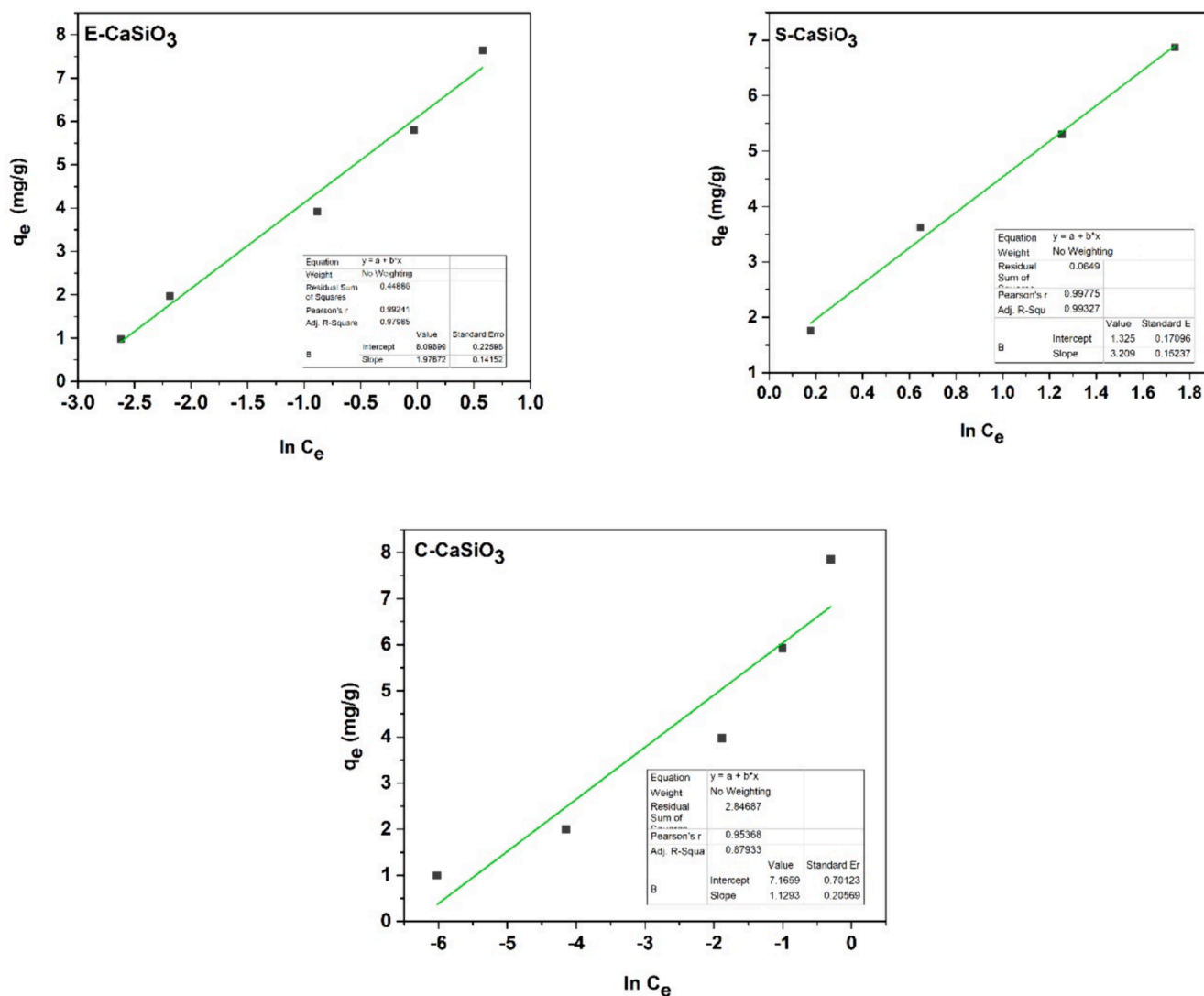
Fig. 16. Graphical representation of Temkin isotherm model of E-CaSiO$_3$, S-CaSiO$_3$, and C-CaSiO$_3$ samples.

Table 7
Data of thermodynamic parameter ΔG^0 (standard Gibbs free energy).

Isotherm model	Fitting of curve	Sample name	Constant	ΔG^0 (KJ/mol)
Langmuir	Linear	E-CaSiO$_3$	1.39382	−0.82267
		S-CaSiO$_3$	0.01045	+11.30585
		C-CaSiO$_3$	113.16044	−11.71604
	Non-linear	E-CaSiO$_3$	1.60597	−1.17369
		S-CaSiO$_3$	0.13716	+4.92196
		C-CaSiO$_3$	5.58132	−4.25999
Freundlich	Linear	E-CaSiO$_3$	5.91643	−4.40446
		S-CaSiO$_3$	1.75081	−1.38763
		C-CaSiO$_3$	8.37587	−5.26571
	Non-linear	E-CaSiO$_3$	5.77164	−4.34307
		S-CaSiO$_3$	2.04386	−1.77106
		C-CaSiO$_3$	8.68647	−5.35593
Temkin	Linear	E-CaSiO$_3$	21.8083	−7.63659
		S-CaSiO$_3$	1.511196	−1.02299
		C-CaSiO$_3$	569.8854	−15.72127

this additional peak was also shown in past research (Harja et al., 2022; Moon et al., 2018). Moreover, in the FTIR spectrum, there were very minor peaks due to the presence of a minor amount of dye in the solution.

4.7.8. XRD analysis after the adsorption and recycling process

XRD analysis of E-CaSiO$_3$ was executed after the adsorption and recycling process and the obtained X-ray diffractogram is represented in Fig. 20. The X-ray diffractogram of E-CaSiO$_3$ after the adsorption and recycling process did not show any discernible change. Consequently, it confirmed that the crystal structure of the adsorbent was unaffected after completing the recycling and adsorption process.

4.7.9. Economic analysis

In this research, we have mainly focused on the synthesis of calcium silicate utilizing waste sources such as eggshells and snail shells. Eggshells and snail shells are utilized as a source of calcium carbonate. Eggshells are one of the most available food-processing waste products, whereas snail shells are natural waste products. So, these two waste products are cost-effective and eco-friendly for industrial-scale applications. Moreover, through the adsorption process, the sample can be utilized several times for removing dye from wastewater.

5. Conclusion

Through a solid-state reaction, calcium silicates were synthesized from three identical sources without using any hazardous chemicals which was confirmed by XRD and FTIR. The crystallite sizes of the

Table 8

Comparison data among various adsorbents from different sources.

| Adsorbent	Source	Adsorbate	Removal percentage (%)	Langmuir maximum adsorption capacity, q_m (mg/g)	Reference
E-CaSiO$_3$	Eggshells	Congo red	98.65	11.59420	This study
S-CaSiO$_3$	Snail shell		98.21	151.28593	
C-CaSiO$_3$	Raw chemical		98.88	4.54318	
Modified chicken feathers	Chicken feathers	Cu (II)	98.9	200	(Chakraborty et al., 2020)
Urea-calcium alginate beads	Brown algae and bivalve shells	Congo red	90.3	441	(Elgarahy et al., 2020)
Modified eggshells	Eggshells	Reactive Blue 198	96.40	0.80	(Zonato et al., 2022)
Calcined eggshells	Eggshells	Basic yellow 28	> 90	28.87	(Slimani et al., 2014)
Modified snail shell	Snail shell	Congo red	95.02	526.31	(Zwier and AL-Da'amy, 2023)
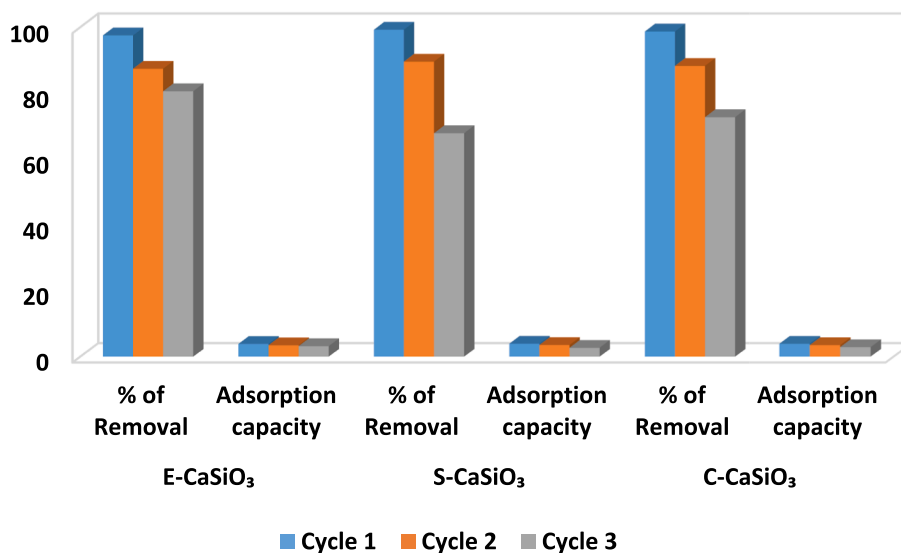
Fig. 17. Regeneration and reusability test of the adsorbents.
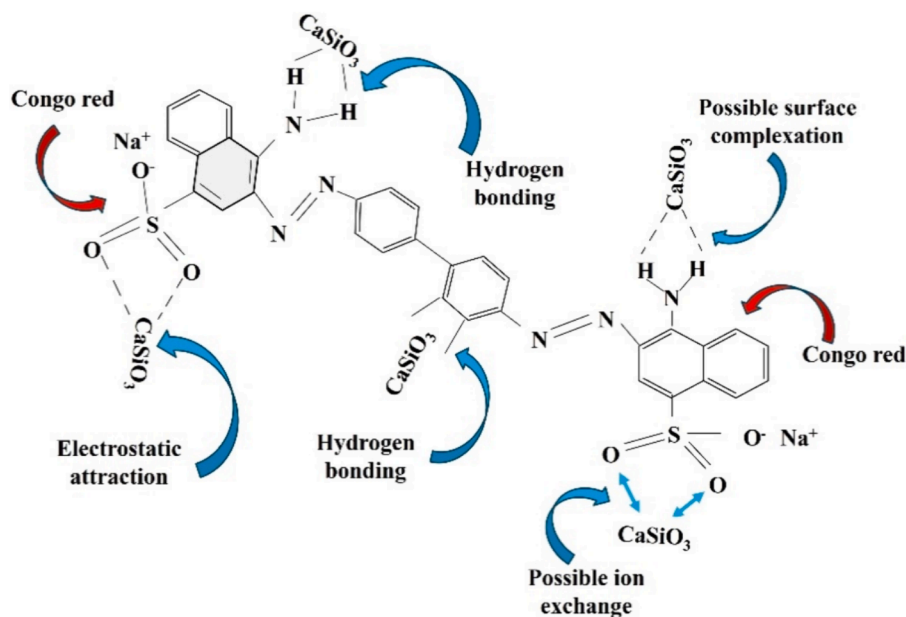

Fig. 18. Congo red dye adsorption mechanism by CaSiO$_3$. (For interpretation of the references to colour in this figure legend, the reader is referred to the web version of this article.)
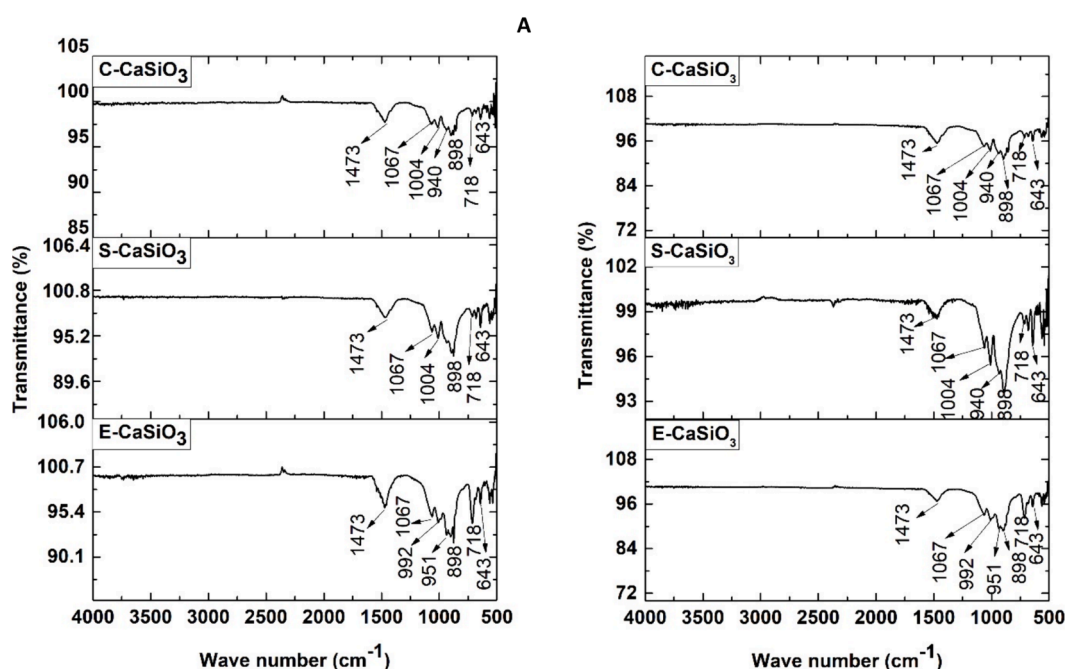
Fig. 19. FTIR spectra of the synthesized adsorbent after adsorption of congo red dye (A) and after recycling process (B).
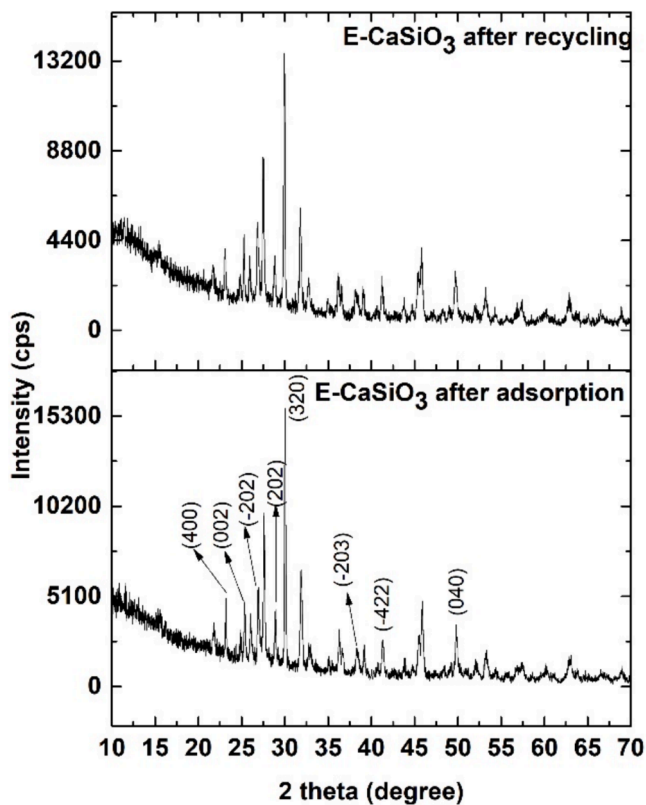

Fig. 20. X-ray diffractogram of E-CaSiO₃ after the adsorption and recycling process.

desired products were less than 80 nm. The adsorption efficacy was impacted by some parameters such as contact time, adsorbent dose, shaking speed, dye concentration, and pH of the solution. The removal percentage for the three types of adsorbents was nearly 100 %. The maximum adsorption capacity (q_m) was 151.28593 mg g^{-1} with Langmuir linear fitting. Moreover, the reusability tests ensured that the adsorbent was cost-effective and eco-friendly. So, this research will attract greater attention because of utilizes food-processing waste (eggshells) and natural waste (snail shells) to synthesize adsorbents that can eradicate anionic congo red dye from wastewater.

CRediT authorship contribution statement

Declaration of competing interest

The authors declare that they have no known competing financial interests or personal relationships that could have appeared to influence the work reported in this paper.

Data availability

Data will be made available on request.

Acknowledgments

Appendix A. Supplementary material

Supplementary data to this article can be found online at https://doi.org/10.1016/j.arabjc.2024.105901.

References

Abd Rashid, R., Shamsudin, R., Abdul Hamid, M.A., Jalar, A., 2014. Low temperature production of wollastonite from limestone and silica sand through solid-state reaction. J. Asian Ceram. Soc. 2, 77–81.

Adebayo M, Jabar J, Amoko J, Openiyi E and Shodiya O 2022 Coconut husk-raw clay-Fe composite: preparation, characteristics and mechanisms of Congo red adsorption *Scientific Reports* **12**.

Adeogun, A.I., Ofudje, E.A., Idowu, M.A., Kareem, S.O., Vahidhabanu, S., Babu, B.R., 2018. Biowaste-derived hydroxyapatite for effective removal of Reactive Yellow 4 dye: Equilibrium, kinetic, and thermodynamic studies. ACS Omega 3, 1991–2000.

Afkhami, A., Moosavi, R., 2010. Adsorptive removal of Congo red, a carcinogenic textile dye, from aqueous solutions by maghemite nanoparticles. J. Hazard. Mater. 174, 398–403.

Ahmad R, Kumar R and Haseeb S 2012 Adsorption of Cu2+ from aqueous solution onto iron oxide coated eggshell powder: Evaluation of equilibrium, isotherms, kinetics, and regeneration capacity *Arabian Journal of Chemistry* **5** 353–9.

Aldahash, S.A., Higgins, P., Siddiqui, S., Uddin, M.K., 2022. Fabrication of polyamide-12/cement nanocomposite and its testing for different dyes removal from aqueous solution: Characterization, adsorption, and regeneration studies. Sci. Rep. 12, 13144.

Al-Degs, Y.S., El-Barghouthi, M.I., El-Sheikh, A.H., Walker, G.M., 2008. Effect of solution pH, ionic strength, and temperature on adsorption behavior of reactive dyes on activated carbon. Dyes Pigm. 77, 16–23.

Ali, N., Said, A., Ali, F., Raziq, F., Ali, Z., Bilal, M., Reinert, L., Begum, T., Iqbal, H.M.N., 2020. Photocatalytic degradation of Congo Red dye from aqueous environment using cobalt ferrite nanostructures: Development, characterization, and photocatalytic performance. Water Air Soil Pollut. 231, 50.

Anirudhan, T.S., Rejeena, S.R., Binusree, J., 2013. Adsorptive separation of myoglobin from aqueous solutions using iron oxide magnetic nanoparticles modified with functionalized nanocrystalline cellulose. J. Chem. Eng. Data 58, 1329–1339.

Anjaneyulu, U., Koppala, S., Swamiappan, S., 2013. Sol-gel combustion synthesis of nanocrystalline Wollastonite by using glycine as a fuel and its in vitro bioactivity studies. Trans. Indian Ceram. Soc. 72, 257–260.

Anon (2) (PDF) Langmuir, Freundlich, Temkin and Dubinin–Radushkevich Isotherms Studies of Equilibrium Sorption of Zn 2+ Unto Phosphoric Acid Modified Rice Husk.

Anon Characterizing the Young's Moduli of Polypropylene–Acicular Wollastonite Crystal Composites: Multiscale Simulation and Experiment | Multiscale Science and Engineering.

Aryee, A.A., Dovi, E., Li, Q., Han, R., Li, Z., Qu, L., 2022. Magnetic biocomposite based on peanut husk for adsorption of hexavalent chromium, Congo red and phosphate from solution: Characterization, kinetics, equilibrium, mechanism and antibacterial studies. Chemosphere 287, 132030.

Bagal M V and Raut-Jadhav S 2021 Chapter 31 - The process for the removal of micropollutants using nanomaterials *Handbook of Nanomaterials for Wastewater Treatment* Micro and Nano Technologies ed B Bhanvase, S Sonawane, V Pawade and A Pandit (Elsevier) pp 957–1007.

Bin Mobarak, M., Pinky, N.S., Chowdhury, F., Hossain, M.S., Mahmud, M., Quddus, M.S., Jahan, S.A., Ahmed, S., 2023. Environmental remediation by hydroxyapatite: Solid state synthesis utilizing waste chicken eggshell and adsorption experiment with Congo red dye. J. Saudi Chem. Soc. 27, 101690.

Bindu P and Thomas S 2014 Estimation of Lattice Strain in ZnO Nanoparticles: X-ray Peak Profile Analysis *Journal of Theoretical and Applied Physics* **8**.

Chakraborty, R., Asthana, A., Singh, A., Yadav, S., Susan, M., Carabineiro, S., 2020. Intensified elimination of aqueous heavy metal ions using chicken feathers chemically modified by a batch method. J. Mol. Liq. 312, 113475.

Diby Paul H S L and Sanjay P Govindwar IJERPH | Free Full-Text | Mineralization and Detoxification of the Carcinogenic Azo Dye Congo Red and Real Textile Effluent by a Polyurethane Foam Immobilized Microbial Consortium in an Upflow Column Bioreactor.

Ebisike K, Elvis Okoronkwo A, Kanayo Alaneme K and Jeremiah Akinribide O 2023 Thermodynamic study of the adsorption of Cd2+ and Ni2+ onto chitosan – Silica hybrid aerogel from aqueous solution *Results in Chemistry* **5** 100730.

Elgarahy, A.M., Elwakeel, K.Z., Mohammad, S.H., Elshoubaky, G.A., 2020. Multifunctional eco-friendly sorbent based on marine brown algae and bivalve shells for subsequent uptake of Congo red dye and copper(II) ions. J. Environ. Chem. Eng. 8, 103915.

Ernawati, L., Wahyuono, R., Dwi Laksono, A., Ningrum, A., Handayani, K., Sabrina, A., 2021. Wollastonite (CaSiO 3)-based composite particles for synthetic food dyes (Brilliant Blue) removal in aquatic media: Synthesis, characterization and kinetic study. IOP Conf. Ser.: Mater. Sci. Eng. 1053, 012001.

Gao H J, Wang S F, Fang L M, Sun G A, Chen X P, Tang S N, Yang H, Sun G Z and Li D F 2021 Nanostructured spinel-type M(M = Mg, Co, Zn)Cr2O4 oxides: novel adsorbents for aqueous Congo red removal *Materials Today Chemistry* **22** 100593.

Ghasemi, M., Ghasemi, M., Ghasemi, N., Khosravi-fard, Y., 2014. A novel agricultural waste based adsorbent for the removal of Pb(II) from aqueous solution: Kinetics, equilibrium and thermodynamic studies. J. Ind. Eng. Chem. 20, 454–461.

Ghosh, S., Sarkar, A., Chatterjee, S., Nayek, H.P., 2021. Elucidation of selective adsorption study of Congo red using new Cadmium(II) metal-organic frameworks: Adsorption kinetics, isotherm and thermodynamics. J. Solid State Chem. 296, 121929.

Habiba, U., Siddique, T.A., Joo, T.C., Salleh, A., Ang, B.C., Afifi, A.M., 2017. Synthesis of chitosan/polyvinyl alcohol/zeolite composite for removal of methyl orange, Congo red and chromium(VI) by flocculation/adsorption. Carbohydr. Polym. 157, 1568–1576.

Han, M., Wang, S., Chen, X., Liu, H., Gao, H., Zhao, X., Wang, F., Yang, H., Yi, Z., Fang, L., 2022. Spinel CuB2O4 (B = Fe, Cr, and Al) oxides for selective adsorption of Congo Red and photocatalytic removal of antibiotics. ACS Appl. Nano Mater. 5, 11194–11207.

Harja, M., Buema, G., Bucur, D., 2022. Recent advances in removal of Congo Red dye by adsorption using an industrial waste. Sci. Rep. 12, 6087.

HENRY M. OTTE Lattice Parameter Determinations with an X-Ray Spectrogoniometer by the Debye-Scherrer Method and the Effect of Specimen Condition | Journal of Applied Physics | AIP Publishing.

Himabindu, B., Latha Devi, N.S.M.P., Rajini Kanth, B., 2021. Microstructural parameters from X-ray peak profile analysis by Williamson-Hall models; A review. Mater. Today: Proc. 47, 4891–4896.

Hossain, M.S., Tuntun, S.M., Bahadur, N.M., Ahmed, S., 2022. Enhancement of photocatalytic efficacy by exploiting copper doping in nano-hydroxyapatite for degradation of Congo Red dye. RSC Adv. 12, 34080–34094.

Hu, J., Deng, W., Chen, D., 2017. Ceria hollow spheres as an adsorbent for efficient removal of acid dye. ACS Sustain. Chem. Eng. 5, 3570–3582.

Jamil, N., Khan, M., Ahsan, N., Anwar, J., Qadir, A., Zameer, M., Shafique, U., 2014. Removal of direct red 16 (textile dye) from industrial effluent by using feldspar. J. Chem. Soc. Pak. 36, 191–197.

Jia, Y., Ding, L., Ren, P., Zhong, M., Ma, J., Fan, X., 2020. Performances and mechanism of Methyl Orange and Congo Red adsorbed on the magnetic ion-exchange resin. J. Chem. Eng. Data 65, 725–736.

Karamanov, A., Pelino, M., 2008. Induced crystallization porosity and properties of sintered diopside and wollastonite glass-ceramics. J. Eur. Ceram. Soc. 28, 555–562.

Kaviti, A.K., Akkala, S.R., 2023. Influence of anodization time on Al2O3 nanoporous morphology and optical properties using energy band gap at room temperature. Results Eng. 17, 100816.

Khorsand Zak A, Abd. Majid W H, Abrishami M E and Yousefi R 2011 X-ray analysis of ZnO nanoparticles by Williamson–Hall and size–strain plot methods *Solid State Sciences* **13** 251–6.

Li H C, Wang D G, Chen C Z, Weng F and Shi H 2016 Influence of different amount of Na 2 O additive on the structure, mechanical properties and degradability of bioactive wollastonite *Ceramics International* **42** 1439–45.

Li, M., Li, J.-T., Sun, H.-W., 2008. Decolorizing of azo dye Reactive red 24 aqueous solution using exfoliated graphite and H2O2 under ultrasound irradiation. Ultrason. Sonochem. 15, 717–723.

Liu H, Wang S, Gao H, Yang H, Wang F, Chen X, Fang L, Tang S, Yi Z and Li D 2022 A simple polyacrylamide gel route for the synthesis of MgAl2O4 nanoparticles with different metal sources as an efficient adsorbent: Neural network algorithm simulation, equilibrium, kinetics and thermodynamic studies *Separation and Purification Technology* **281** 119855.

Mir, F.A., 2014. Transparent wide band gap crystals follow indirect allowed transition and bipolaron hopping mechanism. Results Phys. 4, 103–104.

K. Mohamed Racik S A and Hamza Irfan Full article: Microstructural evaluation of CoAl2O4 nanoparticles by Williamson–Hall and size–strain plot methods.

Monshi, A., Foroughi, M.R., Monshi, M.R., 2012. Modified Scherrer equation to estimate more accurately nano-crystallite size using XRD. WJNSE 02, 154–160.

Moon, S., Salunke, B., Saha, P., Deshmukh, A., Kim, B.S., 2018. Comparison of dye degradation potential of biosynthesized copper oxide, manganese dioxide, and silver nanoparticles using Kalopanax pictus plant extract. Korean J. Chem. Eng. 35.

Nasiri S, Rabiei M, Palevicius A, Janusas G, Vilkauskas A, Nutalapati V and Monshi A 2023 Modified Scherrer equation to calculate crystal size by XRD with high accuracy, examples Fe2O3, TiO2 and V2O5 *Nano Trends* **3** 100015.

Nasiri-Tabrizi, B., 2014. Thermal treatment effect on structural features of mechano-synthesized fluorapatite-titania nanocomposite: A comparative study. J. Adv. Ceram. 3, 31–42.

Nath, H., Saikia, A., Goutam, P.J., Saikia, B.K., Saikia, N., 2021. Removal of methylene blue from water using okra (*Abelmoschus esculentus* L.) mucilage modified biochar. Bioresour. Technol. Rep. 14, 100689.

Nath, D., Singh, F., Das, R., 2020. X-ray diffraction analysis by Williamson-Hall, Halder-Wagner and size-strain plot methods of CdSe nanoparticles- a comparative study. Mater. Chem. Phys. 239, 122021.

Nodehi, R., Shayesteh, H., Kelishami, A.R., 2020. Enhanced adsorption of congo red using cationic surfactant functionalized zeolite particles. Microchem. J. 153, 104281.

Palakurthy S, K. V G R, Samudrala R K and P. A A 2019 In vitro bioactivity and degradation behaviour of β-wollastonite derived from natural waste *Materials Science and Engineering: C* **98** 109–17.

Phuttawong, R., Chantaramee, N., Pookmanee, P., Puntharod, R., 2015. Synthesis and characterization of calcium silicate from rice husk ash and shell of snail Pomacea Canaliculata by solid state reaction. Adv. Mat. Res. 1103, 1–7.

Pinky, N.S., Mobarak, M., Mustafi, S., Rahman, M., Nahar, A., Saha, T., Bahadur, N., 2023. Facile preparation of micro-porous biochar from Bangladeshi sprouted agricultural waste (corncob) via in-house built heating chamber for cationic dye removal. Arab. J. Chem. 16, 105080.

Prabhu, Y., Rao, K., Kumar, S.S., Kumari, B., 2014. X-ray analysis by Williamson-Hall and size-strain plot methods of ZnO nanoparticles with fuel variation. World J. Nano Sci. Eng. 04, 21–28.

Rabiei, M., Palevicius, A., Monshi, A., Nasiri, S., Vilkauskas, A., Janušas, G., 2020. Comparing methods for calculating nano crystal size of natural hydroxyapatite using X-ray diffraction. Nanomaterials 10, 1627.

Sahadat Hossain, Md., Ahmed, S., 2023. Easy and green synthesis of TiO2 (Anatase and Rutile): Estimation of crystallite size using Scherrer equation, Williamson-Hall Plot, Monshi-Scherrer Model, Size-Strain Plot, Halder- Wagner Model. Results Mater. 20, 100492.

Sahadat Hossain, Md., Ahmed, S., 2023. Crystallographic characterization of naturally occurring aragonite and calcite phase: Rietveld refinement. J. Saudi Chem. Soc. 27, 101649.

Sahadat Hossain Md, Jahan S A and Ahmed S 2023 Crystallographic characterization of bio-waste material originated CaCO3, green-synthesized CaO and Ca(OH)2 *Results in Chemistry* **5** 100822.

Salihi I U, Bala N, Danlami N and Abdulfatah A Y Comparison of Linear and Non-Linear Methods of Freundlich and Langmuir Isotherm Models for the Adsorption of Lead Using Sugarcane Bagasse.

Shayesteh H, Rahbar-Kelishami A and Norouzbeigi R 2016 Evaluation of natural and cationic surfactant modified pumice for congo red removal in batch mode: Kinetic, equilibrium, and thermodynamic studies *Journal of Molecular Liquids* **221** 1–11.

Slimani, R., El Ouahabi, I., Abidi, F., El Haddad, M., Regti, A., Laamari, M.R., Antri, S.E., Lazar, S., 2014. Calcined eggshells as a new biosorbent to remove basic dye from aqueous solutions: Thermodynamics, kinetics, isotherms and error analysis. J. Taiwan Inst. Chem. Eng. 45, 1578–1587.

Thool, G.S., Singh, A.K., Singh, R.S., Gupta, A., Susan, M.A.B.H., 2014. Facile synthesis of flat crystal ZnO thin films by solution growth method: A micro-structural investigation. J. Saudi Chem. Soc. 18, 712–721.

Vichaphund, S., Kitiwan, M., Atong, D., Thavorniti, P., 2011. Microwave synthesis of wollastonite powder from eggshells. J. Eur. Ceram. Soc. 31, 2435–2440.

Vinod Kumar S S (PDF) X-ray Analysis of NiFe 2 O 4 Nanoparticles by Williamson-Hall and Size-Strain Plot Method.

Vitek, R., Masini, J.C., 2023. Nonlinear regression for treating adsorption isotherm data to characterize new sorbents: Advantages over linearization demonstrated with simulated and experimental data. Heliyon 9, e15128.

Wang S, Li M, Gao H, Yin Z, Chen C, Yang H, Fang L, Jagadeesha Angadi V, Yi Z and Li D 2023 Construction of CeO2/YMnO3 and CeO2/MgAl2O4/YMnO3 photocatalysts and adsorption of dyes and photocatalytic oxidation of antibiotics: Performance prediction, degradation pathway and mechanism insight *Applied Surface Science* **608** 154977.

Wang S, Liu H, Li M, Han M, Gao H, Yang H, Fang L, Zhang H, Jagadeesha Angadi V, Manjunatha S O, Cai C and Li D 2023 Various carbon-based MgAl2O4 adsorbents and their removal efficiency of CR dye and antibiotics in aqueous media: High selective adsorption capacity, performance prediction and mechanism insight *Ceramics International* **49** 26734–46.

Wang, S.F., Tang, S.N., Gao, H.J., Yu, C., Yang, H., Yu, X.L., Chen, X.P., Fang, L.M., Li, D. F., 2023. Removal of Congo Red from wastewater using ZnO/MgO nanocomposites as adsorbents: Equilibrium isotherm analyses, kinetics and thermodynamic studies. J. Nano Res. 77, 65–86.

You Y, KeqiQu, Huang Z, Ma R, Shi C, Li X, Liu D, Dong M and Guo Z 2019 Sodium alginate templated hydroxyapatite/calcium silicate composite adsorbents for efficient dye removal from polluted water *International Journal of Biological Macromolecules* **141** 1035–43.

Zhao, K., Wang, X., Chen, T., Wu, H., Li, J., Yang, B., Li, D., Wei, J., 2017. Bisphenol A adsorption properties of mesoporous CaSiO3@SiO2 grafted nonwoven polypropylene fiber. Ind. Eng. Chem. Res. 56, 2549–2556.

Zonato R de O, Estevam B R, Perez I D, Aparecida dos Santos Ribeiro V and Boina R F 2022 Eggshell as an adsorbent for removing dyes and metallic ions in aqueous solutions *Cleaner Chemical Engineering* **2** 100023.

Zwier F B and AL-Da'amy M A 2023 preparation and evaluation of thermodynamics studies of congo red dye adsorption onto chemically modified snail, *journal of aeronautical materials,* **6(3)** 367-375.